

pubs.acs.org/JCTC Article

Simulating Absorption Spectra of Multiexcitonic Systems via Quasiclassical Mapping Hamiltonian Methods

Xing Gao, Yifan Lai, and Eitan Geva*



Cite This: *J. Chem. Theory Comput.* 2020, 16, 6465–6480

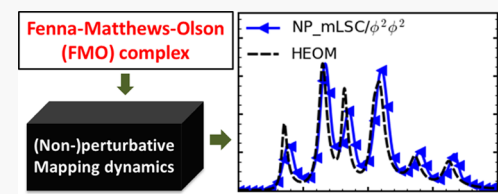


ACCESS I

III Metrics & More

Article Recommendations

ABSTRACT: In this paper, we compare the ability of different quasiclassical mapping Hamiltonian methods to accurately simulate the absorption spectra of multiexcitonic molecular systems. Two distinctly different approaches for simulating the absorption spectra are considered: (1) a perturbative approach, which relies on the first-order perturbation theory with respect to the field-matter interaction; (2) a nonperturbative approach, which mimics the experimental measurement of the absorption spectra from the free-induction decay that follows



a short laser pulse. The methods compared are several variations of the linearized semiclassical (LSC) method, the symmetrical quasiclassical (SQC) method, and the mean-field (Ehrenfest) method. The comparison is performed in the context of a biexcitonic model and a seven-excitonic model of the Fenna–Matthews–Olson (FMO) complex. The accuracy of the various methods is tested by comparing their predictions to the quantum-mechanically exact results obtained via the hierarchy of the equations of motion (HEOM) method, as well as to the results based on the Redfield quantum master equation. The results show that the LSC-based quasiclassical mapping Hamiltonian methods can yield the accurate and robust absorption spectra in the high-temperature and/or slow-bath limit, where the nuclear degrees of freedom can be treated as classical.

1. INTRODUCTION

Optical spectroscopy has long been recognized as a sensitive probe of molecular structure and dynamics. Arguably, the ultimate goal is to translate the spectra into as detailed as possible description of the underlying molecular structure and dynamics. To this end, it is necessary to compare the experimental spectra with the simulated spectra obtained based on a model of the molecular system.

In the case of electronic spectroscopy, the spectra are often simulated based on models with electronic potential energy surfaces (PESs) that are harmonic and identical, except for shifts in equilibrium geometry and energy. ^{1,28–35} Within such models, the entire information regarding the underlying molecular structure and dynamics is given in terms of spectral density functions. ^{1,36} The spectral density functions can be determined in a variety of ways, including empirically (by fitting to experiment), via electronic structure calculations, ^{28–35} or based on transition frequency correlation functions obtained from equilibrium classical molecular dynamics (MD) simulations. ^{32–35}

Even though the above-mentioned harmonic models can often be parameterized so as to reproduce experimental signals rather well and provide useful insight into their molecular origins, they are still based on a rather restrictive set of assumptions that at the very least need to be validated. Furthermore, the spectral density functions represent a rather indirect and nonintuitive connection to the underlying molecular structure and dynamics. Thus, an approach for modeling the spectra, which is not limited to harmonic model

Hamiltonians and is straightforward to apply to complex molecular systems, would be highly desirable. $^{11,13,16-19,24,40-43}$ In this paper, we consider such an approach, which is based on the quasiclassical mapping Hamiltonian (QC/MH) methods.

QC/MH methods 44-67 are based on representing the electronic population and coherence operators, whose expectation values correspond to the diagonal and off-diagonal electronic density matrix elements, respectively, in terms of mapping operators. The latter have the same commutation relations as the original electronic operators. However, unlike the original operators, they are given in terms of auxiliary position and momentum operators, and as such have a welldefined classical limit. Within the QC approximation, one typically treats the nuclear coordinates and momenta, as well as the above-mentioned auxiliary coordinates and momenta associated with the electronic degrees of freedom (DOF), as classical-like. The dynamics of those phase-space variables is then dictated by classical-like Hamilton equations, with the Hamiltonian given by the classical limit of the mapped Hamiltonian in terms of the coordinates and momenta associated with the nuclear and electronic DOF. It should be

Received: July 7, 2020 Published: September 2, 2020





noted that such QC/MH methods are most useful for the study of large systems, especially in the condensed phase, that involve a large number of electronic and/or nuclear DOF, and for which quantum-mechanically exact methods are not feasible due to their exponential scaling with the system size. 68

Various QC/MH methods have been proposed, which differ with respect to the choice of mapping variables, as well as the sampling used to determine the values of the corresponding electronic variables at different times throughout the dynamics. The goal of this paper is to present a comprehensive comparison of the ability of different QC/MH methods to accurately simulate the absorption spectra of the multiexcitonic molecular systems. It should be noted that several related recent papers have already considered the aspects of this question. One recent study by Provazza and Coker provided an analysis of the ability of the symmetrical quasiclassical (SQC) QC/MH method $^{51-56,69}$ to simulate the linear absorption spectra of a biexciton model using a perturbative strategy with respect to the field-matter interaction. 43 Other recent studies by Polley and Loring were based on combining SQC with their optimized mean trajectory approximation to simulate the two-dimensional vibronic spectra. 41,42 In the current paper, we extend the analysis to other QC/MH methods using both perturbative and nonperturbative approaches.

The remainder of this paper is organized as follows. The theory underlying the dynamics of the multiexcitonic systems, QC/MH methods, and the simulation of the absorption spectra is outlined in Section 2. The biexciton and seven-exciton benchmark models are described in Section 3. The results are presented and discussed in Section 4. A summary of the main results is provided in Section 5.

2. THEORY

2.1. Preliminary Considerations. We consider a system with a total Hamiltonian, $\hat{H}(t)$, given by a sum of a time-independent field-free molecular term, \hat{H}_M , and a time-dependent field-matter interaction term, $\hat{W}(t)$

$$\hat{H}(t) = \hat{H}_{M} + \hat{W}(t) \tag{1}$$

We assume that the molecular system comprises of M coupled two-state chromophores with similar excitation energies (in the sense that the difference between the excitation energies of different chromophores is much smaller than the excitation energies themselves). The corresponding field-free multi-excitonic molecular Hamiltonian is given by (in what follows, boldfaced variables, for example $\bf A$, indicate vector quantities, and a hat over a variable, for example $\hat{\bf B}$, indicates an operator quantity)

$$\hat{H}_{M} = H_{0}(\hat{\mathbf{R}}, \hat{\mathbf{P}})|0\rangle\langle0| + \sum_{j=1}^{M} H_{j}(\hat{\mathbf{R}}, \hat{\mathbf{P}})|j\rangle\langle j|$$

$$+ \sum_{j',j=1}^{M} V_{j'j}(\hat{\mathbf{R}})|j'\rangle\langle j|\rangle$$
(2)

Here, M is the number of chromophores; $\hat{\mathbf{R}} = \{\hat{R}_1, \hat{R}_2, ..., \hat{R}_{N_n}\}$ and $\hat{\mathbf{P}} = \{\hat{P}_1, \hat{P}_2, ..., \hat{P}_{N_n}\}$ are the mass-weighted coordinates and momenta operators of the N_n nuclear DOF; $|0\rangle \equiv |0,0,...,0\rangle$ is the uncoupled electronic ground state (all chromophores are in their ground state); $|j\rangle = |0,...,0,1,0...,0\rangle$, with 1 in the jth place, is the uncoupled singly excited electronic state, where the jth chromophore is excited and the rest of the chromophores are in

the ground state; $\hat{H}_0(\hat{\mathbf{R}}, \hat{\mathbf{P}}) = \hat{\mathbf{P}}^2/2 + V_0(\hat{\mathbf{R}})$ are the nuclear Hamiltonians that correspond to the ground electronic state; $\{\hat{H}_j(\hat{\mathbf{R}}, \hat{\mathbf{P}}) = \hat{\mathbf{P}}^2/2 + V_j(\hat{\mathbf{R}})\}$ are the nuclear Hamiltonians that correspond to the uncoupled singly excited electronic states (j = 1,...,M); $\{V_{j'j}(\hat{\mathbf{R}})\}$ are the coupling terms between the chromophores ($\hat{\mathbf{R}}$ -independent if the Condon approximation is applicable).

The field-matter interaction term is given by

$$\hat{W}(t) = -\hat{\boldsymbol{\mu}} \cdot \mathbf{E}(t) \cos[\omega t - \mathbf{kr}]$$
(3)

Here, $\mathbf{E}(t)$, \mathbf{k} , and ω are the pulse envelope, wave vector, and leading frequency of the driving field and $\hat{\boldsymbol{\mu}} = (\hat{\mu}_x, \hat{\mu}_y, \hat{\mu}_z)$ is the dipole moment vector operator of the molecular system. Assuming that the laser frequency is in resonance with the ground state-to-singly excited-band transitions, the dipole moment operator is assumed to be given by

$$\hat{\boldsymbol{\mu}} = \sum_{j=1}^{M} \left[\boldsymbol{\mu}_{0j} |0\rangle\langle j| + \boldsymbol{\mu}_{j0} |j\rangle\langle 0| \right]$$
(4)

Here, $\{\mu_{0j}\}$ are the transition dipole moments (assumed to be $\hat{\mathbf{R}}$ -independent within the Condon approximation).

Substituting eq 4 into eq 3 and performing the rotating wave approximation (RWA),¹ we can rewrite the field-matter interaction term in the following form

$$\hat{W}(t) = -\frac{\hbar}{2} \sum_{j=1}^{M} \left[\chi_{0j}(t) e^{i\omega t - i\mathbf{k}\mathbf{r}} |0\rangle \langle j| + \chi_{j0}(t) e^{-i\omega t + i\mathbf{k}\mathbf{r}} |j\rangle \langle 0| \right]$$
(5)

Here, $\{\hbar\chi_{0j}(t) = \hbar\chi_{j0}^*(t) = \mu_{0j}\cdot\mathbf{E}(t)\}$ are the Rabi frequencies associated with the transitions between the uncoupled ground and the singly excited states.

It should be noted that the uncoupled electronic basis states, $\{|0\rangle, |1\rangle,...,|M\rangle\}$, are assumed to be **R**-independent and that writing the dipole operator in terms of transitions between them represents one choice. Another reasonable choice could be based on writing the dipole operator in terms of the Rdependent eigenstates of the molecular Hamiltonian (the adiabatic basis). Physically meaningful observables such as spectra should be clearly independent of the choice of electronic basis. It should be noted that while calculating the transition dipole moments of the individual chromophores is more convenient in practice, the appropriateness of such an approach becomes questionable in the case of strong coupling (i.e., when $V_{i'i}(\mathbf{R})$ becomes comparable to the transition frequencies of the individual chromophores), where writing the dipole operators in terms of transitions between the eigenstates of the molecular Hamiltonian would be more appropriate. Thus, the form of the transition dipole in eq 4 implicitly assumes that the coupling between the chromophores is weak enough to make this an appropriate description.

2.2. Mixed Quantum-Classical Dynamics in the Rotating Frame. The QC/MH methods under consideration in this paper correspond to a subset of mixed quantum-classical methods, which are based on treating the nuclear DOF as classical-like. To this end, we assume that the dynamics of the electronic DOF is governed by a quantum-mechanical Hamiltonian of the following form

$$\begin{split} \hat{H}_{\text{el}}(\mathbf{R}_{t}, t) &= V_{0}(\mathbf{R}_{t})|0\rangle \langle 0| + \sum_{j=1}^{M} V_{j}(\mathbf{R}_{t})|j\rangle \langle j| + \\ &\sum_{j',j=1}^{M} V_{j'j}(\mathbf{R}_{t})|j'\rangle \langle j| \\ -\frac{\hbar}{2} \sum_{j=1}^{M} \left[\chi_{0j}(t) \mathrm{e}^{\mathrm{i}\omega t - \mathrm{i}\mathbf{k}\mathbf{r}}|0\rangle \langle j| + \chi_{j0}(t) \mathrm{e}^{-\mathrm{i}\omega t + \mathrm{i}\mathbf{k}\mathbf{r}}|j\rangle \langle 0| \right] \end{split}$$

$$(6)$$

Here, \mathbf{R}_t are the nuclear coordinates, which are now described as classical-like and explicitly time-dependent. The actual classical nuclear trajectory, \mathbf{R}_t , depends on the choice of the mixed quantum-classical method. Furthermore, obtaining a physically meaningful result typically requires averaging over an ensemble of such classical trajectories. ^{66,70}

In the next step, we define the electronic density operator in the rotating frame, $\tilde{\sigma}(t)$

$$\tilde{\sigma}(t) = e^{i\hat{H}_{rot}t/\hbar}\hat{\sigma}(t)e^{-i\hat{H}_{rot}t/\hbar}$$
(7)

Here, $\hat{H}_{\rm rot} = \hbar\omega\sum_{j=1}^{M}|j\rangle\langle j| \equiv \hbar\omega[\hat{1}-|0\rangle\langle 0|]$. It should be noted that $\sigma_{jk} = \tilde{\sigma}_{jk}$, except for $\sigma_{j0} = \tilde{\sigma}_{j0} {\rm e}^{-{\rm i}\omega t}$ and $\sigma_{0k} = \tilde{\sigma}_{0k} {\rm e}^{{\rm i}\omega t}$ when $j,k \neq 0$, respectively. The equation of motion for $\tilde{\sigma}(t)$ is given by

$$\frac{\mathrm{d}}{\mathrm{d}t}\tilde{\sigma}(t) = -\frac{i}{\hbar}[\tilde{H}_{\mathrm{el}}(\mathbf{R}_{t}, t), \tilde{\sigma}(t)] \tag{8}$$

where

$$\begin{split} \tilde{H}_{\rm el}(\mathbf{R}_t,\,t) &= V_0(\mathbf{R}_t) |0\rangle \, \langle 0| + \sum_{j=1}^M \, \hbar \Delta_j(\mathbf{R}_t) |j\rangle \langle j| + \\ & \sum_{j',j=1}^M \, V_{j'j}(\mathbf{R}_t)) |j'\rangle \langle j| \end{split}$$

$$-\frac{\hbar}{2} \sum_{j=1}^{M} \left[\chi_{0j}(t) e^{-i\mathbf{k}\mathbf{r}} |0\rangle \langle j| + \chi_{j0}(t) e^{i\mathbf{k}\mathbf{r}} |j\rangle \langle 0| \right]$$
(9)

Here, $\Delta_j(\mathbf{R}_t) = V_j(\mathbf{R}_t)/\hbar - \omega$ is the instantaneous detuning (the deviation of the transition frequency between the ground and excited states of the *j*th chromophore from resonance with the leading frequency of the laser pulse). The main reason for working in the rotating frame is the elimination of the rapidly oscillating factors in the field-matter interaction term, $e^{\pm i\omega t}$ (compare eqs 6 and (9)).

Several interesting limits of the Hamiltonian in eq 9 are noteworthy:

- In the case of a laser pulse with a square envelope, χ_{0j} is constant while the pulse is on.
- The weak impulsive limit⁶ corresponds to the case where the pulse is much shorter than the time scale of nuclear motion, such that \mathbf{R}_t does not change during the time that the pulse is on. Thus, if the time origin, t = 0, coincides with the time that the pulse is turned on

$$\begin{split} \tilde{H}_{\text{el}}(\mathbf{R}_{t}, t) &\rightarrow V_{0}(\mathbf{R}_{0})|0\rangle \langle 0| + \sum_{j=1}^{M} \hbar \Delta_{j}(\mathbf{R}_{0})|j\rangle \langle j| + \\ &\sum_{j',j=1}^{M} V_{j'j}(\mathbf{R}_{0})|j'\rangle \langle j| \\ -\frac{\hbar}{2} \sum_{j=1}^{M} \left[\chi_{0j}(t) \mathrm{e}^{-\mathrm{i}\mathbf{k}\mathbf{r}}|0\rangle \langle j| + \chi_{j0}(t) \mathrm{e}^{\mathrm{i}\mathbf{k}\mathbf{r}}|j\rangle \langle 0| \right] \end{split} \tag{10}$$

so that the only time dependence of $\tilde{H}_{\rm el}$ comes from $\mathbf{E}(t)$.

• The strong impulsive limit corresponds to the case where in addition to the pulse being much shorter than the time scale of nuclear motion, the pulse amplitude, E(t), is large enough so that the dynamics is dominated by the field-matter interaction term. In this case, the Hamiltonian while the pulse is on is given by

$$\tilde{H}_{el}(\mathbf{R}_{t}, t) \rightarrow -\frac{\hbar}{2} \sum_{j=1}^{M} \left[\chi_{0j}(t) e^{-i\mathbf{k}\mathbf{r}} |0\rangle \langle j| + \chi_{j0}(t) e^{i\mathbf{k}\mathbf{r}} |j\rangle \langle 0| \right]$$
(11)

2.3. Mapping Hamiltonian (MH) Approach and Quasiclassical (QC) Approximation. For the purpose of this paper, we can restrict ourselves to an initial state of the overall system (electronic + nuclear DOF) of the single-product form

$$\hat{\rho}(0) = \hat{\rho}_n(0) \otimes \hat{\sigma}(0) = \sum_{j,j'} \sigma_{j'j}(0) \hat{\rho}_n(0) |j'\rangle\langle j|$$
(12)

Here, $\hat{\sigma}(0) \equiv \sum_{j,j'} \sigma_{j'j}(0) |j'\rangle\langle j|$ and $\hat{\rho}_n(0)$ are the initial electronic and nuclear density operators, respectively. Given this initial state, the electronic reduced density matrix elements at a later time t are given by

$$\begin{split} \sigma_{j'j}(t) &= \sum_{k,k'} \sigma_{kk'}(0) \mathrm{Tr}\{\hat{\rho}_n(0)|k\rangle\langle k'|\hat{U}^{\dagger}(t)|j\rangle\langle j'|\hat{U}(t)\} \\ &\equiv \sum_{k,k'} \sigma_{kk'}(0) C_{\hat{M}_{kk'},\hat{M}_{jj'}}(t) \end{split} \tag{13}$$

where $\hat{U}(t)$ is the time evolution operator, $\hat{M}_{ii'} = |j\rangle\langle j'|$, and

$$C_{\hat{A}\hat{B}}(t) = \text{Tr}\{\hat{\rho}_n(0)\hat{A}\hat{U}^{\dagger}(t)\hat{B}\hat{U}(t)\}$$
(14)

It should be noted that \hat{A} and \hat{B} in eq 14 are purely electronic operators. Thus, calculating $\hat{\sigma}(t)$ calls for calculating the correlation functions $\{C_{\hat{M}_{kk},\hat{M}_{jj'}}(t)\}$. It should also be noted that $\{\hat{M}_{jj'}\}$ correspond to electronic population operators and $\{\hat{M}_{jj'}\}$, with $j \neq j'$, correspond to electronic coherence operators. Thus, there are four kinds of correlation functions: (1) population—population (k = k' and j = j'); (2) coherence—coherence $(k \neq k' \text{ and } j \neq j')$; (3) coherence—population $(k \neq k' \text{ and } j = j')$; and (4) population—coherence $(k = k' \text{ and } j \neq j')$.

 $\{\sigma_{j'j}(t)\}$ can also be written in terms of other sets of correlation functions. One such alternative set, which is particularly useful in the context of the MH/QC methods, is based on writing the electronic population operator $\hat{M}_{jj} = |j\rangle\langle j|$ as the sum of the identity operator, $\hat{1}$, and the traceless operator $\hat{Q}_j^{57,58}$

Table 1. Five LSC-Based QC/MH Methods Used in This Paper

methods based on set #1 in eq 20					
$C_{[\hat{M}_{kk'}]_W[\hat{M}_{y'}]_W}(t)$					
method	$[\hat{M}_{kk'}]_W$ mapping	$egin{aligned} [\hat{M}_{jj'}]_W ext{ mapping} \ [\hat{M}_{jj'}]_W^{(1)}(\mathbf{q},\mathbf{p}) \end{aligned}$			
LSCI	$[\hat{M}_{kk'}]_W^{ ext{(II)}}(\mathbf{q},\mathbf{p})$	$[\hat{M}_{jj'}]^{(\mathbf{I})}_W(\mathbf{q},\mathbf{p})$			
LSCII	$[\hat{M}_{kk'}]_W^{ ext{(II)}}(\mathbf{q},\mathbf{p})$	$[\hat{M}_{jj'}]^{ ext{(II)}}_{W}(\mathbf{q},\mathbf{p})$			
methods based on set #2 in eq 20					

	$C_{[\hat{A}]_W[\hat{B}]_W}(t)$			
method	$[\hat{A}]_W$		$[\hat{B}]_W$	
	$[\hat{1}]_W$ mapping	$[\hat{Q}_k]_W$ mapping	$[\hat{Q}_{j}]_{W}$ mapping	$[\hat{M}_{jj'}]_W$ mapping
$mLSC/\phi^1\phi^1$	1	$[\hat{Q}_k]_W^{(\mathrm{I})}(\mathbf{q},\mathbf{p})$	$[\hat{Q}_j]_W^{(\mathrm{II})}(\mathbf{q},\mathbf{p})$	$[\hat{M}_{jj'}]_W^{\mathrm{(II)}}(\mathbf{q},\mathbf{p})$
$mLSC/\phi^1\phi^2$	1	$[\hat{Q}_k]_W^{ ext{(II)}}(\mathbf{q,p})$	$[\hat{Q}_j]_W^{(\mathrm{II})}(\mathbf{q},\mathbf{p})$	$[\hat{M}_{jj'}]_W^{(\mathrm{II})}(\mathbf{q},\mathbf{p})$
$mLSC/\phi^2\phi^2$	$2\hbar\phi(\mathbf{q},\mathbf{p})$	$[\hat{Q}_k]_W^{\mathrm{(II)}}(\mathbf{q},\mathbf{p})$	$[\hat{Q}_j]_W^{(\mathrm{II})}(\mathbf{q},\mathbf{p})$	$[\hat{M}_{jj'}]_W^{\mathrm{(II)}}(\mathbf{q},\mathbf{p})$

 ${}^{a}[\hat{M}]_{W}^{(1)}$ is given in eq 25, $[\hat{M}]_{W}^{(II)}$ is given in eq 26, $[\hat{Q}]_{W}$ is given in eq 28, $\phi(\mathbf{q}, \mathbf{p})$ is given in eq 27, and the general form of $C_{A_{W}B_{W}}(t)$ is given in eq 23.

$$\hat{M}_{jj} = \frac{1}{N_{\rm e}} (\hat{1} + \hat{Q}_{j}) \tag{15}$$

where $N_e = M + 1$ (the overall number of the electronic states) and

$$\hat{Q}_{j} = N_{e} \hat{M}_{jj} - \sum_{j'=0}^{M} \hat{M}_{j'j'}$$
(16)

This then gives rise to the following alternative expressions for the population–population, population–coherence, and coherence–population correlation functions (the coherence–coherence correlation function remains the same as $C_{\hat{M}_{kk'},\hat{M}_{jj'}}(t)$ since it does not involve a population operator)

$$C_{\hat{M}_{kk},\hat{M}_{jj}}(t) = \frac{1}{N_e^2} [N_e + C_{\hat{1},\hat{Q}_j}(t) + C_{\hat{Q}_k,\hat{Q}_j}(t)]$$
(17)

$$C_{\hat{M}_{kk},\hat{M}_{jj}}(t) = \frac{1}{N_e} [C_{\hat{1},\hat{M}_{jj}}(t) + C_{\hat{Q}_k,\hat{M}_{jj}}(t)]$$
(18)

$$C_{\hat{M}_{kk'},\hat{M}_{jj}}(t) = \frac{1}{N_e} C_{\hat{M}_{kk'}\hat{Q}_j}(t)$$
(19)

Thus, $\hat{\sigma}(t)$ can be obtained from two different sets of correlation functions

set #1: {
$$C_{\hat{M}_{kk},\hat{M}_{jj}}(t)$$
, $C_{\hat{M}_{kk'},\hat{M}_{jj}}(t)$, $C_{\hat{M}_{kk},\hat{M}_{jj}}(t)$, $C_{\hat{M}_{kk'},\hat{M}_{jj'}}(t)$ }
set #2: { $C_{\hat{1},\hat{Q}_{j}}(t)$, $C_{\hat{Q}_{k'},\hat{Q}_{j}}(t)$, $C_{\hat{M}_{kk'}\hat{Q}_{j}}(t)$, $C_{\hat{M}_{kk'},\hat{M}_{jj'}}(t)$ }
$$(20)$$

Both sets will yield the exact quantum results if the correlation functions are calculated fully quantum mechanically. However, this need not be the case when approximations methods are used to evaluate the correlation functions (see below).

2.3.1. Methods Based on the Linearized Semiclassical (LSC) Approximation. The MH methods are based on casting the population and coherence operators, $\{\hat{M}_{ij'} = |j\rangle\langle j'|\}$, onto an isomorphic set of operators, $\{M_{ij'}(\hat{\mathbf{q}},\hat{\mathbf{p}})\}$

$$|j\rangle \langle j'| \rightarrow M_{jj'}(\hat{\mathbf{q}}, \, \hat{\mathbf{p}})$$
 (21)

with $\{M_{jj'}(\hat{\mathbf{q}},\hat{\mathbf{p}})\}$ satisfying the same commutation relations as $\{|j\rangle\langle j'|\}$. Here, $\{\hat{\mathbf{q}},\hat{\mathbf{p}}\}$ are a set of auxiliary Cartesian coordinates and momenta operators. Thus, in terms of

the mapping operators, the correlation function $C_{\hat{A}\hat{B}}(t)$ (see eq 14) is given by

$$C_{\hat{A}\hat{B}}(t) = \operatorname{Tr}\{\hat{\rho}_n(0)A(\hat{\mathbf{q}}, \hat{\mathbf{p}})B(\hat{\mathbf{q}}_t, \hat{\mathbf{p}}_t)\}$$
(22)

where, $\hat{\mathbf{q}}_t = \hat{\mathbf{U}}^{\dagger}(t) \; \hat{\mathbf{q}}\hat{\mathbf{U}}(t) \; \text{and} \; \hat{\mathbf{p}}_t = \hat{\mathbf{U}}^{\dagger}(t)\hat{\mathbf{p}}\hat{\mathbf{U}}(t).$

Applying the LSC approximation^{78–80} to a correlation function in eq 22 results in the following QC approximation for $C_{\hat{A}\hat{B}}(t)$

$$C_{A_W B_W}(t) = \left(\frac{1}{2\pi\hbar}\right)^F \int \mathbf{dR}_0 \int \mathbf{dP}_0 \int \mathbf{dq}_0$$
$$\int \mathbf{dp}_0 \times [\hat{\rho}_n(0)]_W(\mathbf{R}_0, \mathbf{P}_0) A_W(\mathbf{q}_0, \mathbf{p}_0) B_W(\mathbf{q}_t, \mathbf{p}_t) \quad (23)$$

Here, $F = N_e + N_n$ is the total number of DOF of the overall system; $[\hat{\rho}_n(0)]_W(\mathbf{R}_0, \mathbf{P}_0)$ is the Wigner transform of the nuclear operator $\hat{\rho}_n(0)$; $A_W(\mathbf{q}_0, \mathbf{p}_0)$ and $B_W(\mathbf{q}_0, \mathbf{p}_t)$ are the Wigner transforms of the electronic operators \hat{A} and \hat{B} , respectively. The general forms of the Wigner transforms of a nuclear operator \hat{D} and an electronic operator \hat{G} are given by

$$D_{W}(\mathbf{R}, \mathbf{P}) = \int d\mathbf{Z} e^{-i\mathbf{Z}\mathbf{P}/\hbar} \left\langle \mathbf{R} + \frac{\mathbf{Z}}{2} \middle| D(\hat{\mathbf{R}}, \hat{\mathbf{P}}) \middle| \mathbf{R} - \frac{\mathbf{Z}}{2} \right\rangle,$$

$$G_{W}(\mathbf{q}, \mathbf{p}) = \int d\mathbf{z} e^{-i\mathbf{z}\mathbf{p}/\hbar} \left\langle \mathbf{q} + \frac{\mathbf{z}}{2} \middle| G(\hat{\mathbf{q}}, \hat{\mathbf{p}}) \middle| \mathbf{q} - \frac{\mathbf{z}}{2} \right\rangle$$
(24)

Applying the QC approximation to the two sets of correlation functions in eq 20 then leads to two alternative implementations of the QC/MH approximation. 57,58,66

The actual choice of the mapping variables is not unique and multiple choices of the mapping variables have been proposed and employed. ^{63,65,69,76,77,81} In this paper, we consider two such choices, which are based on the Stock—Thoss—Meyer—Miller mapping ^{44,45} (the reader is referred to refs 66 and 82 for a more detailed discussion of these two choices). The first choice, which we refer to as mapping #1, leads to the following QC mapping variables

$$[\hat{M}_{jj}]_{W}^{(1)}(\mathbf{q}, \mathbf{p}) = \frac{1}{2\hbar} (q_{j}^{2} + p_{j}^{2} - \hbar)$$

$$[\hat{M}_{jj'}]_{W}^{(1)}(\mathbf{q}, \mathbf{p}) = \frac{1}{2\hbar} (q_{j} - ip_{j}) (q_{j'} + ip_{j'})$$
(25)

where $j \neq j'$. The second choice, which we refer to as mapping #2, leads to the following QC mapping variables

$$[\hat{M}_{jj}]_{W}^{(II)}(\mathbf{q}, \mathbf{p}) = \phi(\mathbf{q}, \mathbf{p}) \left(q_{j}^{2} + p_{j}^{2} - \frac{\hbar}{2} \right)$$

$$[\hat{M}_{jj'}]_{W}^{(II)}(\mathbf{q}, \mathbf{p}) = \phi(\mathbf{q}, \mathbf{p}) (q_{j} - ip_{j}) (q_{j'} + ip_{j'})$$
(26)

where $j \neq j'$ and

$$\phi(\mathbf{q}, \mathbf{p}) = \frac{2^{N_e+1}}{\hbar} \exp \left[-\frac{1}{\hbar} \sum_{j=0}^{M} (q_j^2 + p_j^2) \right]$$
(27)

We also note that the QC mapping #1 and mapping #2 approximations for \hat{Q}_i , eq 16, are given by

$$[\hat{Q}_{j}]_{W}^{(I)}(\mathbf{q}, \mathbf{p}) = N_{e}[\hat{M}_{jj}]_{W}^{(I)}(\mathbf{q}, \mathbf{p}) - \sum_{j'=0}^{M} [\hat{M}_{j'j'}]_{W}^{(I)}(\mathbf{q}, \mathbf{p}),$$

$$[\hat{Q}_{j}]_{W}^{(II)}(\mathbf{q}, \mathbf{p}) = N_{e}[\hat{M}_{jj}]_{W}^{(II)}(\mathbf{q}, \mathbf{p}) - \sum_{j'=0}^{M} [\hat{M}_{j'j'}]_{W}^{(II)}(\mathbf{q}, \mathbf{p})$$
(28)

Applying the above-mentioned QC/MH approximations to the two sets of correlation functions in eq 20 yields the five different LSC-based methods shown in Table 1 (see refs 57, 58, 66 for a more detailed discussion). The first two methods, LSCI (also referred to as PBME⁷⁵) and LSCII (also referred to as LSC- IVR^{46}), are based on set #1 of correlation functions (see eq 20). Both LSCI and LSCII use mapping #2 for $[\hat{M}_{kk}]_W$ and $[\hat{M}_{kk'}]_W$ but differ from each other in the mapping used for $[\hat{M}_{ii}]_W$ and $[\hat{M}_{ii'}]_W$, with LSCI using mapping #1 and LSCII using mapping #2. The third through fifth LSC-based methods are based on set #2 of correlation functions (see eq 20).⁵⁷ For the correlation functions $C_{[\hat{1}]_{W}[\hat{Q}_{i}]_{W'}}$ $C_{[\hat{1}]_{W}[\hat{M}_{ij'}]_{W'}}$ $C_{[\hat{Q}_{k}]_{W}[\hat{Q}_{i}]_{W'}}$ and $C_{[\hat{Q}_{k}]_{W}[\hat{M}_{ij'}]_{W'}}$ all three methods use mapping #2 for $[\hat{Q}_i]_W$ and $[\hat{M}_{ii'}]_W$ but differ in how they map the unity operator and in the mapping used for $[\hat{Q}_k]_W$. The third method, referred to as mLSC/ $\phi^1\phi^1$, maps the unity operator onto 1 and uses mapping #1 for $[\hat{Q}_k]_W$. The fourth method, referred to as mLSC/ $\phi^1\phi^2$, maps the unity operator onto 1 and uses mapping #2 for $[\hat{Q}_k]_W$. The fifth method, referred to as mLSC/ $\phi^2\phi^2$, maps the unity operator onto $2\hbar\phi(\mathbf{q},\mathbf{p})$ [with $\phi(\mathbf{q},\mathbf{p})$ given in eq 27] and uses mapping #2 for $[\hat{Q}_k]_{W}$.

To obtain the correlation functions in eq 20, the nuclear and electronic coordinates and momenta at time t, $\{\mathbf{R}_v, \mathbf{P}_v, \mathbf{q}_v, \mathbf{p}_t\}$, need to be obtained from the initial state $\{\mathbf{R}_0, \mathbf{P}_0, \mathbf{q}_0, \mathbf{p}_0\}$. The initial nuclear coordinates and momenta, $\{\mathbf{R}_0, \mathbf{P}_0\}$, are sampled from the Wigner transform of the initial nuclear density matrix. The initial electronic coordinates and momenta, $\{\mathbf{q}_0, \mathbf{p}_0\}$, are sampled based on the phase-space density $\phi(\mathbf{q}_0, \mathbf{p}_0)$ or $\phi^2(\mathbf{q}_0, \mathbf{p}_0)$ (see Table 1). $\{\mathbf{R}_v, \mathbf{P}_v, \mathbf{q}_v, \mathbf{p}_t\}$ is obtained from $\{\mathbf{R}_0, \mathbf{P}_0, \mathbf{q}_0, \mathbf{p}_0\}$ via classical dynamics as dictated by the following symmetrized mapping Hamiltonian 44,50

$$\begin{split} H(\mathbf{R},\,\mathbf{P},\,\mathbf{q},\,\mathbf{p}) &= \frac{\mathbf{P}^2}{2} + \overline{V}(\mathbf{R}) \\ &+ \frac{1}{2\hbar} [V_0 - \overline{V}](\mathbf{R}) (q_0^2 + p_0^2) \\ &+ \frac{1}{2} \sum_{j=1}^M \left[\Delta_j - \overline{V} \right](\mathbf{R}) (q_j^2 + p_j^2) \\ &+ \frac{1}{2\hbar} \sum_{jj'}^M V_{jj'}(\mathbf{R}) (q_j - ip_j) (q_{j'} + ip_{j'}) \\ &- \frac{1}{4} \sum_{j=1}^M \left[\chi_{0j}(t) \mathrm{e}^{-\mathrm{i}\mathbf{k}\mathbf{r}} (q_0 - ip_0) (q_j + ip_j) \right. \\ &+ \chi_{j0}(t) \mathrm{e}^{\mathrm{i}\mathbf{k}\mathbf{r}} (q_j - ip_j) (q_0 + ip_0)] \end{split}$$

It should be noted that the symmetrized form of the mapping Hamiltonian, eq 29, is obtained by shifting the diagonal elements in the Hamiltonian by $\overline{V} = \frac{1}{N_{\rm e}} \left[V_0 + \sum_{j=1}^M \hbar \Delta_j \right]$ and using the closure relation, $\sum_{j=0}^M |j\rangle\langle j| = \hat{1}$.

2.3.2. Symmetrical Quasiclassical (SQC) Method. The SQC method can be viewed as an alternative implementation of the LSC approximation. S1-56 Within SQC, each electronic state $|j\rangle$ is associated with a classical harmonic mode whose state is described by an action variable, n_j , and an angle variable, u_j . The QC mapping variables for the electronic density matrix elements in terms of action—angle (aa) variables are given by

$$[\hat{M}_{jj}]_W^{(\text{SQC})}(\mathbf{n},\,\mathbf{u}) = \delta(n_j - 1) \prod_{\substack{\xi = 0 \\ f \neq j}}^M \delta(n_\xi) ,$$

$$[\hat{M}_{jj'}]_{W}^{(\text{SQC})}(\mathbf{n}, \mathbf{u}) = e^{i(u_{j'} - u_{j})} \delta\left(n_{j} - \frac{1}{2}\right) \delta\left(n_{j'} - \frac{1}{2}\right) \prod_{\substack{\xi = 0 \\ \xi \neq j, j'}}^{M} \delta(n_{\xi})$$
(30)

where $\mathbf{n} = (n_0,...,n_M)$ and $\mathbf{u} = (u_0,...,u_M)$. The SQC method is based on replacing the delta function $\delta(n_j - a)$ with the prelimit delta function $h(\gamma - |n_j - a|)/2\gamma$, where

$$h(x) = \begin{cases} 1 & x \ge 0 \\ 0 & x < 0 \end{cases} \tag{31}$$

is the Heaviside function and γ is the window width parameter (set to 0.366, as recommended in ref 51).

It should be noted that the above prescription corresponds to the implementation of SQC in terms of fixed square sampling windows. Other implementations in terms of triangular⁵⁵ and adjustable⁸³ windows have also been proposed, but will not be considered here for the sake of brevity.

Within SQC, initial nuclear coordinates and momenta are sampled based on $[\hat{\rho}_n(0)]_W(\mathbf{R}_0, \mathbf{P}_0)$ (the same as in the LSC-based methods). Initial sampling of the action variable, n_i , is done randomly within the corresponding square sampling window. Initial sampling of the angle variables, $\{u_j\}$, is done randomly within the interval $(0, 2\pi)$.

The dynamics of the a-a variables within SQC is identical to that in the LSC-based methods when translated into Cartesian

coordinates and momenta. The relationship between the a-a variables and the Cartesian coordinates and momenta is given by

$$q_{j} = \sqrt{2(n_{j} + \gamma)\hbar} \cos(u_{j}),$$

$$p_{j} = \sqrt{2(n_{j} + \gamma)\hbar} \sin(u_{j})$$
(32)

Similar to LSC, the correlation function $C_{\hat{A}\hat{B}}(t)$ in SQC is calculated based on the following QC approximation

$$C_{A_W B_W}(t) = \left(\frac{1}{2\pi\hbar}\right)^F \int d\mathbf{R}_0 \int d\mathbf{P}_0 \int d\mathbf{n}_0 \int d\mathbf{u}_0$$
$$\times [\hat{\rho}_n(0)]_W(\mathbf{R}_0, \mathbf{P}_0) A_W(\mathbf{n}_0, \mathbf{u}_0) B_W(\mathbf{n}_t, \mathbf{u}_t)$$
(33)

2.3.3. Mean-Field (Ehrenfest) Method. The mean-field (MF) method can also be cast as a QC/MH-type method. 44 More specifically, assuming that the initial electronic state corresponds to a pure state, $|\psi(0)\rangle$, for a given nuclear trajectory R_{ν} , the electronic state at a later time t is given by

$$|\psi(t; \mathbf{R}_t)\rangle = \sum_{j=0}^{M} a_j(t; \mathbf{R}_t)|j\rangle$$
(34)

It should be noted that even though the initial electronic state is given by $|\psi(0)\rangle$ for all nuclear trajectories, different nuclear trajectories will give rise to different $|\psi(t; \mathbf{R}_t)\rangle$.

The corresponding electronic density matrix at time t is then obtained by averaging over the ensemble of the nuclear trajectories, which is achieved by averaging over the initial conditions of the nuclear coordinates and momenta based on the Wigner distribution of the initial nuclear density operator

$$\hat{\sigma}(t) = \left(\frac{1}{2\pi\hbar}\right)^{N_n} \int \mathbf{d}\mathbf{R}_0 \int \mathbf{d}\mathbf{P}_0[\hat{\rho}_n(0)]_W(\mathbf{R}_0, \mathbf{P}_0)$$

$$\sum_{j,k=0}^M a_j(t; \mathbf{R}_t) a_k^*(t; \mathbf{R}_t) |j\rangle \langle k|$$
(35)

Expressing the expansion coefficients in terms of the Cartesian coordinates and momenta as follows

$$a_j = \frac{1}{\sqrt{2}}(q_j + ip_j) \tag{36}$$

it can then be shown that the MF (Ehrenfest) method is equivalent to propagating $\{\mathbf{R}_{v}, \mathbf{P}_{v}, \mathbf{q}_{v}, \mathbf{p}_{t}\}$ as classical variables whose dynamics is governed by the QC Hamiltonian in eq 29. The initial nuclear coordinates and momenta within the MH method are sampled in the same way as the LSC and SQC methods. However, unlike the LSC and SQC methods, the initial values of the electronic coordinates and momenta, $\{\mathbf{q}_{0}, \mathbf{p}_{0}\}$, are uniquely determined by $\{a_{i}(0)\}$.

It should be noted that the version of the MF method used here requires that the initial electronic state is described by a pure state. We will therefore limit the use of the MF method to cases where the initial electronic state is of this form.

2.4. Linear Spectroscopy. In this section, we outline two different approaches to calculating the absorption spectrum via the QC/MH methods: (1) The perturbative approach, which is commonly used for simulating the absorption spectrum, and is based on explicitly treating the field-matter interaction as a small perturbation within the first-order (linear) perturbation theory; (2) The nonperturbative approach, which is based on mimicking the experimental procedure used to measure the absorption

lineshape. Ideally, the perturbative and nonperturbative approaches would yield the same result if the calculation is performed in a way that is quantum-mechanically exact and the assumptions underlying the first-order perturbation theory are valid. However, this is not necessarily the case when the approximate methods, like the QC/MH methods described in Section 2.3, are employed. Furthermore, validation of the consistency of the assumptions underlying the first-order perturbation theory calls for comparing the perturbative prediction with a nonperturbative prediction. Both issues are addressed by the protocols for calculating the linear spectra outlined in this section and the comparison of the absorption lineshapes that they give rise to when applied to the model systems in the next section.

2.4.1. Perturbative Approach. The perturbative approach is based on the following expression for the absorption cross section in terms of the linear optical response function (ORF)¹

$$\kappa(\omega) = \frac{2\pi}{n(\omega)} \operatorname{Im} \int_0^\infty \mathrm{d}t e^{\mathrm{i}\omega t} S^{(1)}(t)$$
(37)

Here, $n(\omega)$ is the index of refraction and $S^{(1)}(t)$ is the linear ORF, which is given by 1

$$S^{(1)}(t) = \frac{1}{3} \frac{i}{\hbar} \theta(t) \sum_{a=x,y,z} \text{Tr}([\hat{\mu}_a(t), \hat{\mu}_a(0)] \hat{\rho}_{eq})$$
(38)

where $\theta(t)$ is a Heaviside step function $(\theta(t) = 0 \text{ or } 1 \text{ when } t < 0 \text{ or } > 0$, respectively), $\hat{\mu}_a(t) = \mathrm{e}^{\mathrm{i}\hat{H}_Mt/\hbar}\hat{\mu}_a\mathrm{e}^{-\mathrm{i}\hat{H}_Mt/\hbar}$, and $\hat{\rho}_{\mathrm{eq}} = \mathrm{e}^{-\hat{\rho}\hat{H}_M}$. It should be noted that (1) $\chi^{(1)}(\omega) = \int_0^\infty \mathrm{d}t \, \mathrm{e}^{\mathrm{i}\omega t} \, \mathrm{d}t \, \mathrm{e}^{\mathrm{i}\omega t} \, \mathrm{d}t \, \mathrm{e}^{\mathrm{i}\omega t} \, \mathrm{e}^{\mathrm{i}\omega t} \, \mathrm{e}^{\mathrm{i}\omega t}$. S(1) is the linear susceptibility, so that the absorption spectrum is proportional to the imaginary part of $\chi^{(1)}(\omega)$; (2) eq 38 assumes that the measurement is performed on an isotropic ensemble of the molecular systems such that all molecular orientations are equally probable; (3) traditionally, the lineshape function is defined without the $1/n(\omega)$ factor and is therefore proportional to $\mathrm{Im}\chi^{(1)}(\omega)$; (4) in practice, the relative height of the absorption peaks is of interest, rather than their absolute values. Thus, when comparing different approaches below, we will always normalize the results so that the maxima of the lineshape are the same.

As is well known, the linear ORF can be written in terms of the imaginary part of the equilibrium dipole—dipole correlation function

$$S^{(1)}(t) = -\frac{2}{\hbar}\theta(t)\text{Im}[J(t)]$$
(39)

where

$$J(t) = \frac{1}{3} \sum_{a=x,y,z} \operatorname{Tr}(\hat{\mu}_a(t)\hat{\mu}_a(0)\hat{\rho}_{eq}) \equiv \frac{1}{3} \operatorname{Tr}(\hat{\boldsymbol{\mu}}(t) \cdot \hat{\boldsymbol{\mu}}(0)\hat{\rho}_{eq})$$

$$\tag{40}$$

is the quantum-mechanical equilibrium dipole—dipole correlation function. Thus, calculating the absorption lineshape within the perturbative approach requires calculating $\mathrm{Im}[J(t)]$ by the QC/MH method of choice, substituting it into eq 39 to obtain $S^{(1)}(t)$ and substituting $S^{(1)}(t)$ into eq 37 to obtain the absorption lineshape. Below, we will label the absorption spectra calculated in this way by PT (for the perturbation theory).

Assuming that the electronic excitation energies of the molecular system under consideration in this paper are much larger than $k_{\rm B}T$ (i.e., $\beta\hbar\omega\gg 1$, see Section 2.1), the equilibrium density operator is given by $\hat{\rho}_{\rm eq}=Z_0^{-1}{\rm e}^{-\beta\hat{H}_0}|0\rangle\langle 0|$, where $Z_0=$

 $\operatorname{Tr}(e^{-\beta \hat{H}_0})$. Substituting this $\hat{\rho}_{eq}$ and the dipole moment operators from eq 4 into eq 40 and remembering that $\langle 0|k\rangle = \langle k|0\rangle = \delta(k,0)$, we obtain the following expression for I(t)

$$J(t) = \frac{1}{3} \sum_{a=x,y,z} \sum_{j,j'=1}^{M} \text{Tr} \left\{ e^{i\hat{H}_{M}t/\hbar} [\mu_{0j',a} | 0 \rangle \langle j' | + \mu_{j'0,a} | j' \rangle \langle 0 | \right]$$

$$e^{-i\hat{H}_{M}t/\hbar} \mu_{j0,a} \frac{e^{-\beta \hat{H}_{0}}}{Z_{0}} | j \rangle \langle 0 | \right\}$$

$$(41)$$

Thus, calculating J(t) within PT calls for calculating the coherence—coherence correlation functions of the form

$$C_{\hat{M}_{0j'},\hat{M}_{j0}}(t) = \text{Tr} \left\{ e^{i\hat{H}_{M}t/\hbar} \hat{M}_{0j'} e^{-i\hat{H}_{M}t/\hbar} \hat{M}_{j0} \frac{e^{-\beta\hat{H}_{0}}}{Z_{0}} \right\},$$

$$C_{\hat{M}_{j'0},\hat{M}_{j0}}(t) = \text{Tr} \left\{ e^{i\hat{H}_{M}t/\hbar} \hat{M}_{j'0} e^{-i\hat{H}_{M}t/\hbar} \hat{M}_{j0} \frac{e^{-\beta\hat{H}_{0}}}{Z_{0}} \right\}$$
(42)

As such, J(t) can be calculated using any of the LSC-based methods and SQC (see Section 2.3). It should be noted that this is not the case for calculating J(t) within PT via the MF method since the initial electronic state does not correspond to a pure state. We will therefore not present the results for the absorption spectrum calculated using MF via the PT approach.

2.4.2. Nonperturbative Approach. The nonperturbative approach mimics the commonly used experimental procedure for obtaining the absorption spectra, which is based on measuring the relaxation of the dipole moment expectation values in response to a short laser pulse. To this end, the system is assumed to start out at thermal equilibrium, which is described by the density operator $\hat{\rho}_{\rm eq} = Z_0^{-1} {\rm e}^{-\beta \hat{H}_0} |0\rangle \langle 0|$. Applying a short light pulse to the system then takes it out of equilibrium, following which one measures the free-induction decay, which corresponds to monitoring the expectation value of the dipole moment operator as the system relaxes back to equilibrium. The absorption spectrum is then given by the imaginary part of the Fourier—Laplace transform of the free-induction decay signal.

For the sake of concreteness, we will assume that the short light pulse has a square envelope, so that $E(t) = E_0$ when $-\tau \le t \le 0$ and zero otherwise. Thus, τ is the pulse length and the free-induction decay signal is measured at $t \ge 0$ (i.e., following the pulse). The expectation value of the dipole operator at time t after the pulse is given by (see eq 4)

$$D(t) = \frac{1}{3} \sum_{a=x,y,z} \sum_{j=1}^{M} \left[\mu_{0j,a} \sigma_{j0}(t) + \mu_{j0,a} \sigma_{0j}(t) \right]$$

$$\equiv \frac{1}{3} \sum_{a=x,y,z} \sum_{j=1}^{M} \left[\mu_{0j,a} C_{\hat{M}_{00}, \hat{M}_{0j}}(t) + \mu_{j0,a} C_{\hat{M}_{00}, \hat{M}_{j0}}(t) \right]$$
(43)

The absorption spectrum is therefore given by

$$I(\omega) = \operatorname{Im} \int_0^\infty \mathrm{d}t D(t) \mathrm{e}^{\mathrm{i}\omega t} \tag{44}$$

It should be noted that the dynamics within the time intervals $(-\tau,0)$ and (0,t) is dictated by $\hat{H}(t)=\hat{H}_M+\hat{W}(t)$ and \hat{H}_M , respectively.

In practice, it is convenient to work in the rotating frame since the Hamiltonian during the time interval when the square envelope pulse is on, $(-\tau,0)$, is time-independent (see Section

2.2). This implies simulating $\{\tilde{\sigma}_{j0}(t) = C_{\tilde{M}_{00}\tilde{M}_{0j}}(t), \tilde{\sigma}_{0j}(t) = C_{\tilde{M}_{00}\tilde{M}_{0j}}(t)\}$ and using the identities $\sigma_{j0}(t) = \tilde{\sigma}_{j0}(t) \mathrm{e}^{-\mathrm{i}\omega t}$ and $\sigma_{0j}(t) = \tilde{\sigma}_{0j}(t) \mathrm{e}^{\mathrm{i}\omega t}$ to obtain the expectation value of the dipole operator at time t in the Schrodinger picture. Importantly, calculating D(t) calls for calculating the population—coherence correlation function $\{C_{\tilde{M}_{00}\tilde{M}_{0j}}(t), C_{\tilde{M}_{00}\tilde{M}_{0j}}(t)\}$ that can be calculated within any of the QC/MH methods (including MF) outlined in Section 2.3. It should be noted that within SQC, the correlation function is further normalized in the following manner 56

$$C_{A_W B_W}(t) \to C_{A_W B_W}(t) / \sum_{j=0}^{M} C_{[\hat{M}_{00}]_W, [\hat{M}_{jj}]_W}(t)$$
 (45)

D(t) needs to coincide with $S^{(1)}(t)$ for the perturbative and nonperturbative approaches to yield the same absorption lineshape (see eqs 44 and 37). It can be shown that the two conditions need to be satisfied for this to be the case: $^{6,84}(1)$ The strong impulsive limit, where the pulse is much shorter than the time scale of nuclear motion and the pulse amplitude, $|\mathbf{E}_0|$, is large enough so that the dynamics while the pulse is on is dominated by the field-matter interaction term (see eq 11). (2) The weak-field limit, according to which $\mathrm{e}^{\pm\mathrm{i}\tilde{W}\tau/\hbar} \approx \hat{1} \pm \mathrm{i}\tilde{W}\tau/\hbar$. For those two conditions to be satisfied simultaneously, the following inequality needs to be valid

$$\frac{\hbar}{\tau} \gg |\hbar \chi_{j0}| \gg |\delta V_0(\mathbf{R})|, |\Delta_j|, |V_{jj}|$$
(46)

Thus, the Rabi frequency needs to be simultaneously smaller than \hbar/τ (the weak-field limit) and larger compared to the fluctuations in the ground state potential energy, $|\delta V_0 (\mathbf{R})|$, detuning, $|\Delta_j|$, and electronic coupling, $|V_{jj'}|$ (the strong impulsive limit). The field parameters used for the model calculations reported in Section 4 were chosen so as to satisfy those conditions.

3. MODELS

In the next section, we compare the absorption spectra calculated by applying the above-mentioned seven methods (LSCI, LSCII, mLSC/ $\phi^1\phi^1$, mLSC/ $\phi^1\phi^2$, mLSC/ $\phi^2\phi^2$, SQC, and MF) to the following benchmark models, for which the quantum-mechanically exact results are known: (1) A Frenkel biexciton model; (2) A Frenkel seven-exciton model for the Fenna–Matthews–Olson (FMO) complex. The Hamiltonian of each system has the form of eq 2. In this section, we outline the above-mentioned models.

3.1. Frenkel Biexciton Model. The Frenkel biexciton model corresponds to the case where the molecular system consists of M=2 chromophores, so that there are $N_e=M+1=3$ electronic states (one ground state, $|0\rangle$, and two singly excited states, $\{|1\rangle,|2\rangle\}$). The PESs for the three electronic states and electronic coupling are given by

$$V_{0}(\mathbf{R}) = \sum_{k=1}^{N} \frac{1}{2} \omega_{k}^{2} R_{k,1}^{2} + \sum_{k=1}^{N} \frac{1}{2} \omega_{k}^{2} R_{k,2}^{2}$$

$$V_{1}(\mathbf{R}) = \epsilon_{1} + \sum_{k=1}^{N} \frac{1}{2} \omega_{k}^{2} (R_{k,1} - D_{k})^{2} + \sum_{k=1}^{N} \frac{1}{2} \omega_{k}^{2} R_{k,2}^{2}$$

$$V_{2}(\mathbf{R}) = \epsilon_{2} + \sum_{k=1}^{N} \frac{1}{2} \omega_{k}^{2} R_{k,1}^{2} + \sum_{k=1}^{N} \frac{1}{2} \omega_{k}^{2} (R_{k,2} - D_{k})^{2}$$

$$V_{12}(\mathbf{R}) = V_{21}(\mathbf{R}) = \Delta$$

$$(47)$$

Here, ϵ_j denotes the minimum-to-minimum excitation energy of the jth chromophore (j=1,2) and Δ is the electronic coupling coefficient (not to be confused with the detuning). Each chromophore has its own set of N=100 uncoupled harmonic modes, $\mathbf{R}_1=(R_{1,1},...,R_{N,1})$ and $\mathbf{R}_2=(R_{1,2},...,R_{N,2})$, so that the optimal geometry is only displaced with respect to those modes when the chromophore is excited. Thus, the overall number of nuclear DOF is $N_n=M\times N=200$. The displacements $\{D_k\}$ are assumed to be the same for each chromophore and are given by $D_k=g_k/\omega_k^2$, where $\{\omega_k\}$ and $\{g_k\}$ are obtained from the Debye spectral density

$$J(\omega) = \frac{\pi}{2} \sum_{k}^{N} \frac{g_{k}^{2}}{\omega_{k}} \delta(\omega - \omega_{k}) \to 2\zeta \frac{\omega \omega_{c}}{\omega^{2} + \omega_{c}^{2}}$$
(48)

following the discretization approach outlined in ref 85. λ and $\omega_{\rm c}$ correspond to the reorganization energy and cutoff frequency.

Below, we report the calculations for this model with ϵ_1 = 50 cm⁻¹, ϵ_2 = -50 cm⁻¹, Δ = 100 cm⁻¹, λ = 50 or 150 cm⁻¹ for (1) $\omega_{\rm c}$ = 18 cm⁻¹ and T = 300 K (the slow-bath and high-temperature case); (2) $\omega_{\rm c}$ = 200 cm⁻¹ and T = 72 K (the fast-bath and low-temperature case). Thus, the ratio of the coupling strength between the electronic and nuclear DOF, measured by λ , and the electronic coupling coefficient, Δ , is given by λ/Δ = 0.5 and 1.5.

We also assume that the laser pulse has a square envelope with leading frequency $\omega=1050~{\rm cm}^{-1}$ and pulse duration $\tau=80$ au = 1.935 fs. The two transition dipole vectors are assumed antiparallel, with the ratio of their magnitude given by $\mu_{01}/\mu_{02}=5$. The Rabi frequencies are assumed to be given by $\chi_{01}=\chi_{10}=2000~{\rm cm}^{-1}$ and $\chi_{02}=\chi_{20}=-400~{\rm cm}^{-1}$. For $\mu_{02}=1$ au, this corresponds to a field strength of \sim 1.17 \times $10^{11}~{\rm W/cm}^2$.

3.2. Frenkel Seven-Exciton Model for FMO. The Frenkel seven-exciton model for FMO was adopted from ref 86 and has been used extensively as a benchmark. ^{87–90} It corresponds to the case where the molecular system consists of M=7 chromophores, so that there are $N_{\rm e}=M+1=8$ electronic states (one ground state, $|0\rangle$, and seven singly excited states, $\{|1\rangle,...,|7\rangle\}$). The PESs for the 8 electronic states are given by

$$V_0(\mathbf{R}) = \sum_{j=1}^{M} \sum_{k=1}^{N} \frac{1}{2} \omega_k^2 R_{k,j}^2$$

$$V_j(\mathbf{R}) = \epsilon_j + \sum_{k=1}^{N} \frac{1}{2} \omega_k^2 (R_{k,j} - D_k)^2 + \sum_{j' \neq j}^{M} \sum_{k=1}^{N} \frac{1}{2} \omega_k^2 R_{k,j'}^2,$$

$$(j, j' > 0)$$
(49)

The chromophores' minimum-to-minimum excitation energies, $\{\epsilon_i\}$, electronic coupling coefficients, $\{V_{jj'}|j_jj'=1,...,7\}$, and

transition dipole moments, $\{\mu_{0j}\}$, were adopted from refs 55, 86, 89, 90. Each chromophore has its own set of N=200 uncoupled harmonic modes, $\mathbf{R}_j=(R_{1,j},...,R_{N,j})$, so that the over number of nuclear DOF is $N_n=M\times N=1400$. All of the transition dipole moment vectors are assumed to have the same magnitude, $|\mu_{01}|=|\mu_{02}|=\cdots|\mu_{07}|=|\mu|$, but are oriented in different directions. The Rabi frequencies are assumed to be given by $\chi=|\mu|$ $|\mathbf{E}_0|=700$ cm⁻¹.

4. RESULTS AND DISCUSSION

In this section, we report the linear spectra for the above-mentioned biexciton and seven-exciton models, calculated via the perturbative and nonperturbative approaches, based on the above-mentioned QC/MH methods (LSCI, LSCII, mLSC/ $\phi^1\phi^1$, mLSC/ $\phi^1\phi^2$, mLSC/ $\phi^2\phi^2$, SQC, and MF). The converged results were obtained by averaging over 10^6 trajectories, with a time step of 10 au \approx 0.24 fs during the pulse and 40 au \approx 0.96 fs during the field-free dynamics that follow it. For comparison, we also present the spectra calculated based on the Redfield method (see Appendix 1).

All approximate methods are compared with the numerically exact results obtained via the hierarchy of equations of motion (HEOM) approach, either via the open-source package pyrho for the biexciton model⁹¹ or from ref 90 for FMO. For the biexciton model, the converged HEOM results at $T=300~\rm K$ were obtained with zero Matsubara frequencies (K=0) via the high-temperature approximation and as many as L=20 levels in the hierarchy. To obtain the converged results at $T=72~\rm K$, a finite truncation depth (L=6) and a finite number of Matsubara frequencies (K=2) were used.

4.1. Frenkel Biexciton Model. For the biexciton model, we start with the slow-bath and high-temperature case ($\omega_c = 18 \text{ cm}^{-1}$, T = 300 K). The absorption spectra for this case as obtained via the NP approach based on different QC/MH methods are shown in Figure 1. Both the time-domain free-

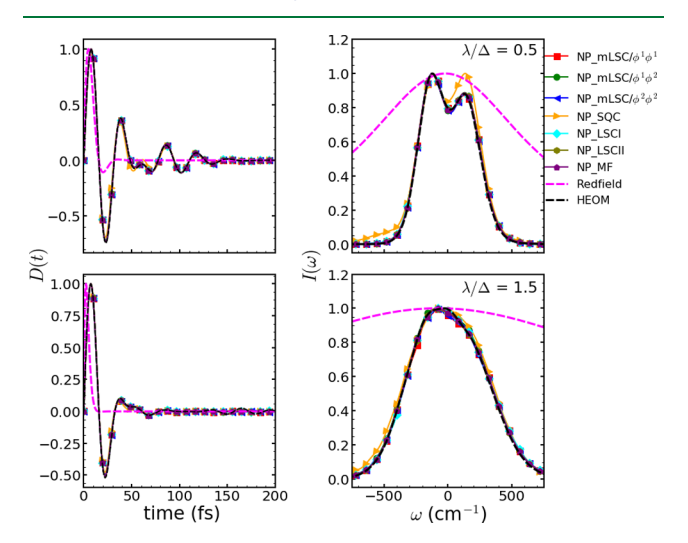


Figure 1. Absorption spectra for the biexciton model at the slow-bath and high-temperature case ($\omega_{\rm c}=18~{\rm cm}^{-1}, T=300~{\rm K}$), as obtained via the NP approach based on different QC/MH methods. Also shown are the Redfield method and numerically exact HEOM method results. Both the time-domain free-induction decay (left panels) and frequency-domain absorption spectrum (right panels) are shown, for $\lambda=50~{\rm cm}^{-1}$ (top panels) and $\lambda=150~{\rm cm}^{-1}$ (bottom panels). The origin of the frequency axis is set to coincide with the light pulse leading frequency. The results were normalized so that the maximum is equal to 1.

induction decay (left panels) and frequency-domain absorption spectrum (right panels) are shown, for $\lambda = 50~{\rm cm}^{-1}$ (top panels) and $\lambda = 150~{\rm cm}^{-1}$ (bottom panels), which correspond to weak and strong coupling between the electronic and nuclear DOF, respectively.

As expected, the free-induction decay is more damped and the absorption spectrum is broader in the strong coupling case. The absorption lineshape predicted by the Redfield method is seen to be significantly broader in comparison to the exact result. This can be traced back to the fact that the slow-bath limit is expected to give rise to strong non-Markovian effects, which cannot be captured by the Markovian Redfield quantum master equation. ⁹²

All QC/MH methods are seen to be able to reproduce the exact absorption spectrum rather well in the slow-bath and hightemperature case. This is consistent with the fact that treating the nuclear DOF as classical is reasonable in the slow-bath and high-temperature limit. Most QC/MH methods are seen to quantitatively reproduce both the positions, widths, and relative heights of the two peaks in the weak coupling limit. Those correspond to transitions between the ground state and each of the two singly excited eigenstates. Thus, their relative heights correspond to the difference in the oscillator strength of those two transitions. SQC is the only method that is unable to correctly reproduce the relative heights of the two peaks. This observation echoes previous observations that SQC with square windows functions can become inaccurate in the weak coupling limit⁵⁶ and when used to calculate coherences, rather than populations. 43 It should be noted that other implementations of SQC that employ triangular windows or adjustable window functions may be able to resolve those discrepancies. 56,83 It is also interesting to note that the discrepancy between SQC and the exact result is much more pronounced in the frequency domain than in the time domain.

The absorption spectra for the slow-bath and high-temperature case ($\omega_{\rm c}=18~{\rm cm^{-1}}$, $T=300~{\rm K}$) as obtained via the PT approach based on the different LSC-based QC/MH methods are shown in Figure 2. The fact that the results obtained via the PT approach are essentially indistinguishable in comparison to the NP approach (see Figure 1) implies that the NP and PT approaches coincide for the field parameters used in this paper. This is not trivial, given that the two approaches use different kinds of correlation functions (population—coherence in the case of NP and coherence—coherence in the case of PT). Thus, the fact that the same results are obtained despite of this is a testimony of the robustness of the LSC-based QC/MH methods and implies that the choice between the PT and NP approaches is a matter of convenience.

Next, we consider the fast-bath and low-temperature case (ω_c = 200 cm⁻¹ and T = 72 K). The absorption spectra for this case as obtained via the NP approach based on different QC/MH methods are shown in Figure 3. Both the time-domain free-induction decay (left panels) and frequency-domain absorption spectrum (right panels) are shown, for λ = 50 cm⁻¹ (top panels) and λ = 150 cm⁻¹ (bottom panels), which correspond to weak and strong coupling between the electronic and nuclear DOF, respectively.

As for the slow-bath and high-temperature case, the free-induction decay is more damped and the absorption spectrum is broader in the strong coupling case. Unlike the slow-bath and high-temperature case, the absorption lineshape is predicted by the Redfield method is seen to be in good agreement with the exact result when $\lambda = 50$ cm⁻¹, which implies that the Markovian

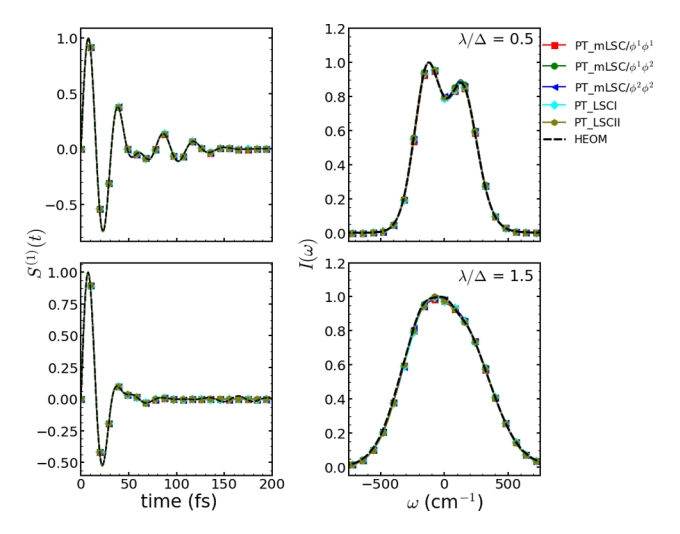


Figure 2. Absorption spectra for the biexciton model at the slow-bath and high-temperature case ($\omega_{\rm c}=18~{\rm cm}^{-1},\,T=300~{\rm K}$), as obtained via the PT approach based on different LSC-based QC/MH methods and the HEOM method. Both the time-domain linear response function (left panels) and frequency-domain absorption spectrum (right panels) are shown, for $\lambda=50~{\rm cm}^{-1}$ (top panels) and $\lambda=150~{\rm cm}^{-1}$ (bottom panels). The origin of the frequency axis is set to coincide with the light pulse leading frequency. The results were normalized so that the maximum is equal to 1.

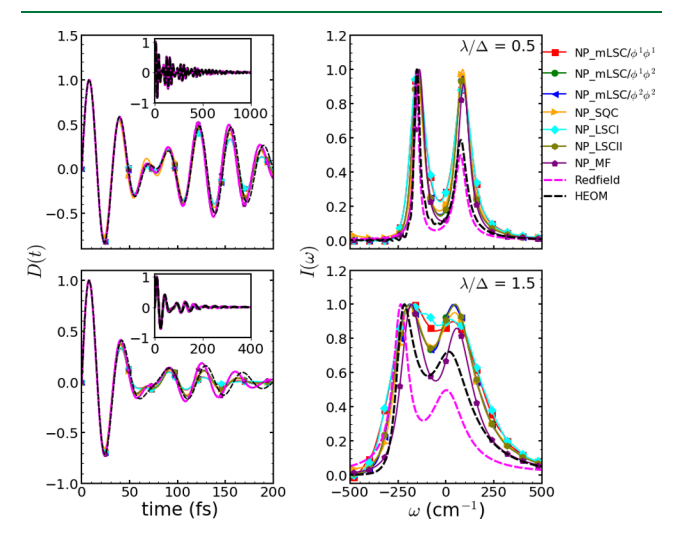


Figure 3. Absorption spectra for the biexciton model at the fast-bath and low-temperature case ($\omega_{\rm c}=200~{\rm cm^{-1}}$, $T=72~{\rm K}$), as obtained via the NP approach based on different QC/MH methods. Also shown are the Redfield method and numerically exact HEOM method results. Both the time-domain free-induction decay (left panels) and frequency-domain absorption spectrum (right panels) are shown, for $\lambda=50~{\rm cm^{-1}}$ (top panels) and 150 cm⁻¹ (bottom panels). The origin of the frequency axis is set to coincide with the light pulse leading frequency. The results were normalized so that the maximum is equal to 1.

approximation is valid in this case and is consistent with the fact that the Redfield method assumes weak coupling between the electronic and nuclear DOF. Indeed, the agreement between the absorption lineshape predicted by the Redfield method and the exact result is seen to deteriorate when $\lambda = 150$ cm⁻¹, which corresponds to stronger coupling between the electronic and nuclear DOF. However, even in this case, the Redfield method is seen to capture the peak positions and widths rather well, with

the main discrepancy between the two corresponding to the relative heights of the two peaks.

In contrast, the various QC/MH methods are seen to be significantly less accurate in the fast-bath and low-temperature case in comparison to the slow-bath and high-temperature case. Whereas the peak locations and widths are reproduced rather well by the QC/MH methods, significant discrepancies are observed with respect to the relative heights of the two peaks. This is consistent with the fact that treating the nuclear DOF as classical is less reasonable in the fast-bath and low-temperature limit. It should be noted that here too, the discrepancies in the frequency domain are more pronounced than in the time domain.

The absorption spectra for the fast-bath and low-temperature case (ω_c = 200 cm⁻¹, T = 72 K) as obtained via the PT approach based on the different LSC-based QC/MH methods are shown in Figure 4. The fact that the results obtained via the PT

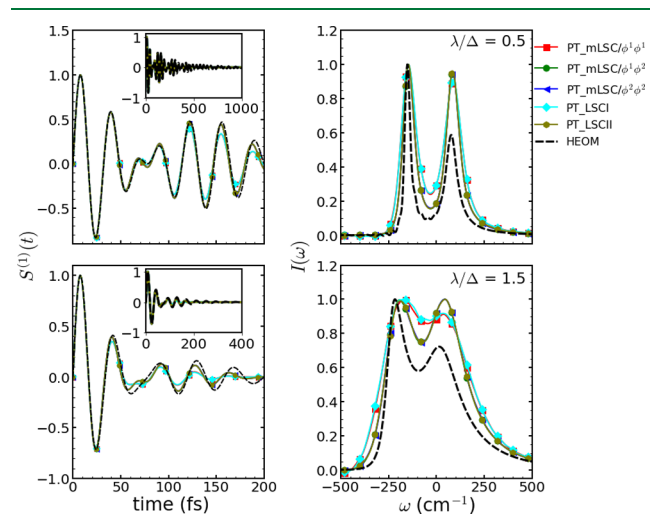


Figure 4. Absorption spectra for the biexciton model at the fast-bath and low-temperature case (ω_c = 200 cm⁻¹, T = 72 K), as obtained via the PT approach based on different LSC-based QC/MH methods and the HEOM method. Both the time-domain linear response function (left panels) and frequency-domain absorption spectrum (right panels) are shown, for λ = 50 cm⁻¹ (top panels) and 150 cm⁻¹ (bottom panels). The origin of the frequency axis is set to coincide with the light pulse leading frequency. The results were normalized so that the maximum is equal to 1.

approach are essentially indistinguishable in comparison to the NP approach (see Figure 3) implies that the NP and PT approaches coincide for the field parameters used in this paper and that the predictions of the LSC-based methods are robust, even when they are less accurate.

4.2. Frenkel Seven-Exciton Model for FMO. The absorption spectra for the seven-exciton model of FMO at T=30,77, and 300 K, as obtained via the NP approach, based on different QC/MH methods, are shown in Figures 5–7, respectively.

The peak locations and widths are seen to be captured rather well by all QC/MH methods even at the lowest temperature (T = 30 K, see Figure 5), which represents the most challenging case for such methods. The main deviations are with respect to the relative peak heights, although peak frequencies are also seen to be visibly shifted. When it comes to relative peak heights, the mLSC methods are observed to be the most accurate, while SQC is observed to be the least accurate. When it comes to peak

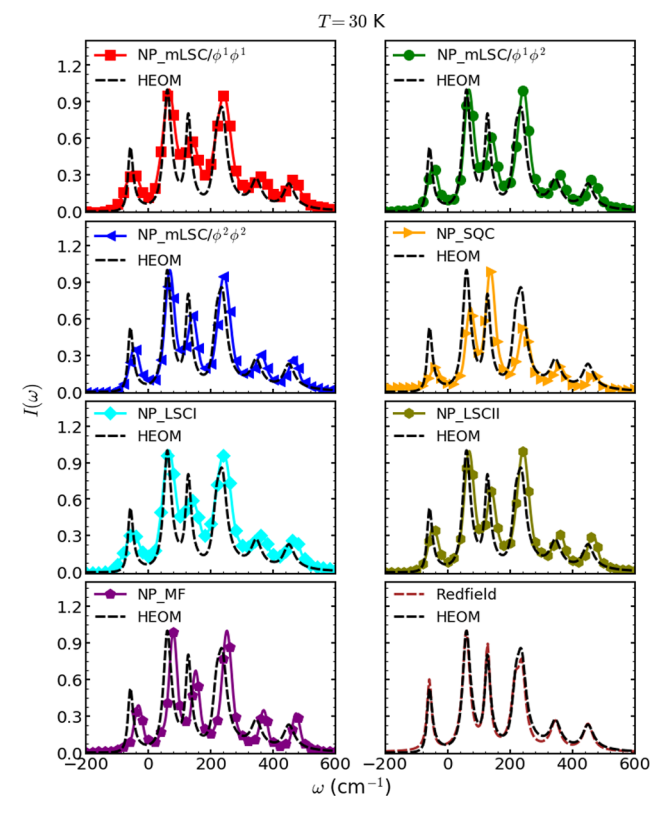


Figure 5. Absorption spectra for the FMO model at $T=30~\rm K$, as obtained via the NP approach, based on different QC/MH methods. Also shown are the Redfield method and numerically exact HEOM method results. ⁹⁰ The origin of the frequency axis is set to coincide with the light pulse leading frequency. The results were normalized so that the maximum is equal to 1.

positions, MF is seen to be the least accurate, while all of the remaining QC/MH methods are observed to be of similar accuracy. It should be noted that the Redfield method is in excellent agreement with the exact result in this case. This suggests that the assumptions of weak coupling between electronic and nuclear DOF and Markovity underlying the Redfield method are valid for FMO at 30 K.

The accuracy of all QC/MH methods improves as the temperature increases from T=30 to 77 K (see Figure 6). With the exception of SQC, all LSC-based methods and the MF method are observed to reproduce the relative peak heights better then they did at T=30 K. With the exception of MF, all LSC-based methods and SQC are observed to reproduce the exact peak location rather well. It should be noted the Redfield method is still in excellent agreement with the exact result at 77 K

Further increasing the temperature to T = 300 K (see Figure 7), the MF- and LSC-based methods all seem to reproduce the exact absorption lineshape rather accurately. This however is not the case for SQC, which can be attributed to its abovementioned inability to reproduce the correct relative peak heights. The Redfield method is also seen to be less accurate in this case, which we attribute to the emergence of non-Markovian effects.

Finally, the absorption spectra calculated via the NP approach are compared to those calculated via the PT approach. To this end, we show the results obtained using mLSC/ $\phi^1\phi^1$, mLSC/ $\phi^1\phi^2$, LSCI and LSCII at T=30,77, and 300 K, in Figures 8–10, respectively. As for the biexciton model, the fact that the results

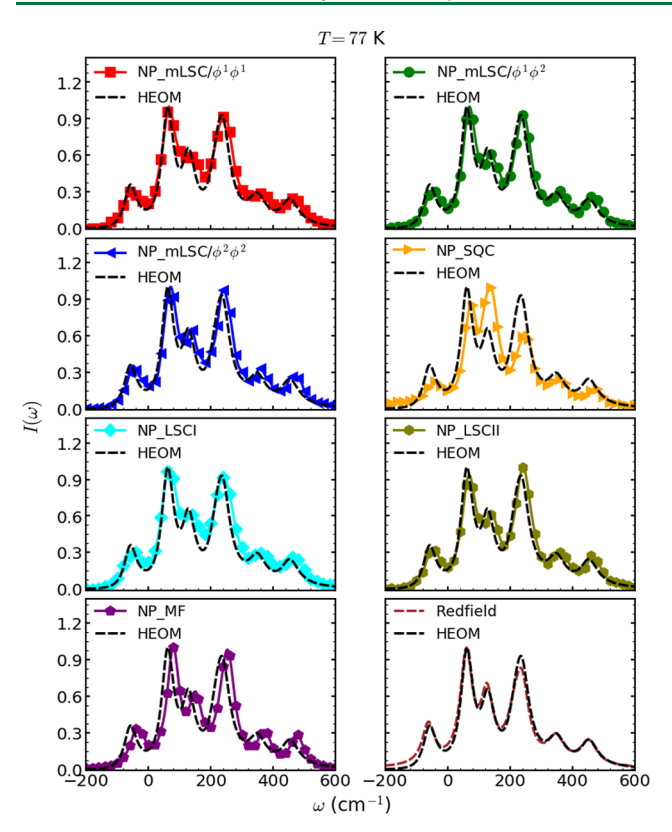


Figure 6. Absorption spectra for the FMO model at $T=77\,$ K, as obtained via the NP approach based on different QC/MH methods. Also shown are the Redfield method and numerically exact HEOM method results. ⁹⁰ The origin of the frequency axis is set to coincide with the light pulse leading frequency. The results were normalized so that the maximum is equal to 1.

obtained via the PT approach are essentially indistinguishable from these obtained via the NP approach implies that the NP and PT approaches coincide for the field parameters used in this paper, and that the predictions of the LSC-based methods are robust.

5. SUMMARY

The QC/MH methods represent a cost-effective computational strategy for simulating the nonadiabatic dynamics of the complex molecular systems characterized by a large number of electronic and/or nuclear DOF. The optical spectra provide some of the most sensitive probes of molecular structure and dynamics of such systems. Thus, the development of the general-purpose computational methods for simulating the optical spectra within the framework of the QC/MH methods represents a natural next step in the advancement of these methods and the expansion of their range of applicability. Recent studies by Provazza and Coker⁴³ and by Polley and Loring^{41,42} have taken first steps toward achieving this goal. In the current paper, we extend the analysis to other QC/MH methods as well as to a nonperturbative approach for calculating the linear spectra of the multiexcitonic molecular systems.

To this end, we performed a comprehensive comparison of the linear spectra obtained via seven different QC/MH approaches (LSCI, LSCII, mLSC/ $\phi^1\phi^1$, mLSC/ $\phi^1\phi^2$, mLSC/ $\phi^2\phi^2$, SQC, and MF) in the context two benchmark models for which numerically exact HEOM results are available (biexciton and seven-exciton models). Also included in the comparison were the results obtained via the Redfield method, which is

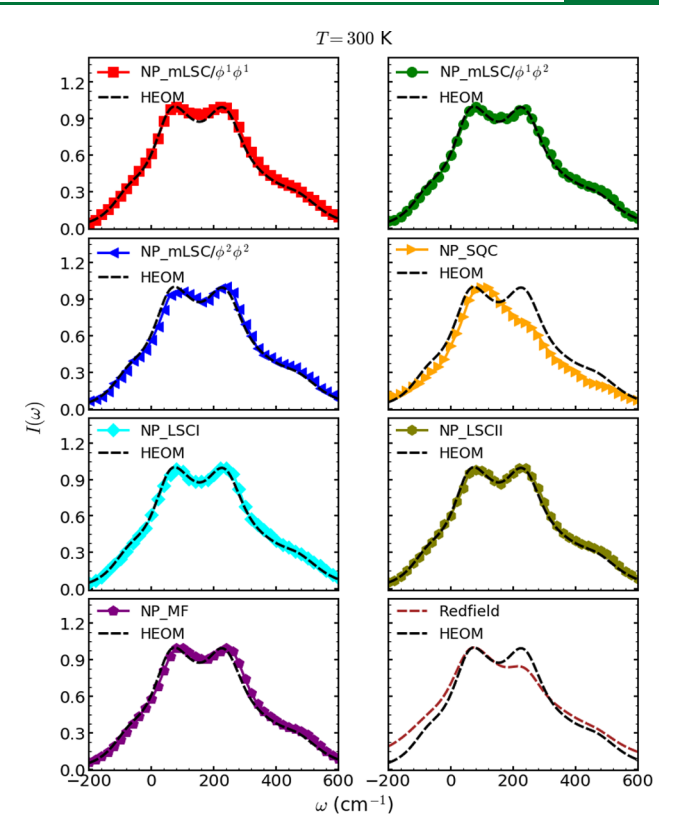


Figure 7. Absorption spectra for the FMO model at $T=300~\rm K$, as obtained via the NP approach based on different QC/MH methods. Also shown are the Redfield method and numerically exact HEOM method results. ⁹⁰ The origin of the frequency axis is set to coincide with the light pulse leading frequency. The results were normalized so that the maximum is equal to 1.

based on treating the nuclear DOF fully quantum mechanically and assuming weak coupling between the electronic and nuclear DOF and describing the dynamics of the electronic density operator in terms of a Markovian quantum master equation.

It should be emphasized that while the benchmark models used here involve harmonic electronic PESs, which are given in terms of uncoupled harmonic modes, the QC/MH approach is not limited to such systems and would in fact be most advantageous for systems described by all-atom anharmonic PESs, for which numerically exact results would not be feasible.

Another aspect considered in this paper is the comparison between the perturbative and nonperturbative approaches to simulating the linear spectra. More specifically, the perturbative approach relies on the first-order perturbation theory with respect to the field-matter interaction, while the nonperturbative approach attempts to mimic the experimental measurement of the absorption spectra from the free-induction decay that follows a short laser pulse. The field parameters used in this paper were chosen so that the results obtained via the PT and NP approaches would coincide if the calculation was carried out in a quantum-mechanically exact manner. The fact that they still coincide when calculated via the approximate QC/MH methods is not trivial, given that the two approaches use different kind of correlation functions (population-coherence in the case of NP and coherence-coherence in the case of PT), and is demonstrative of the robustness of the QC/MH methods. It also implies that the choice between the PT and NP approaches is a matter of convenience, at least for the models under consideration in this paper. However, the NP approach does

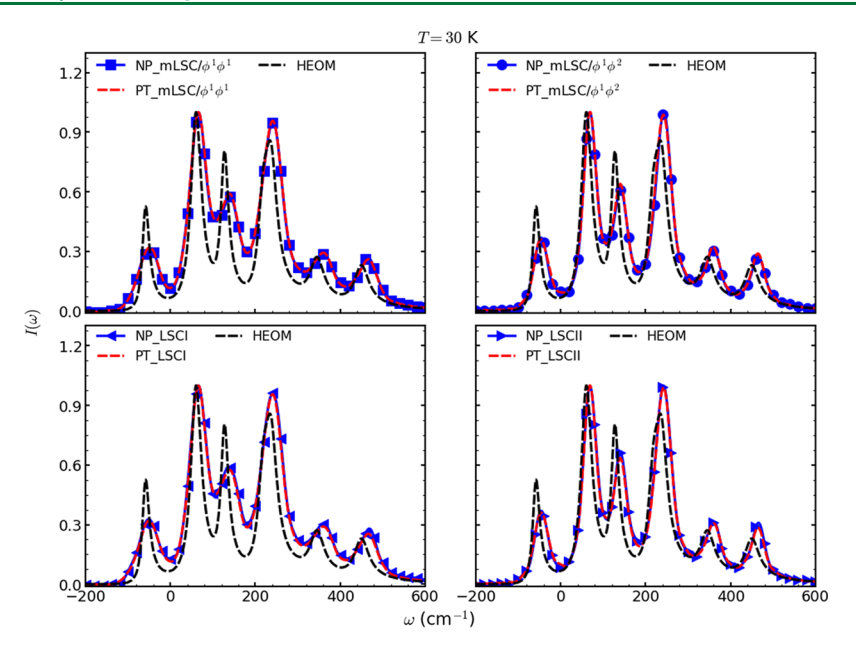


Figure 8. Comparison of the absorption spectra for the FMO model at T = 30 K, as obtained via the PT and NP approaches, based on the indicated QC/MH methods. Also shown numerically the exact HEOM method results obtained via the PT approach. ⁹⁰ The origin of the frequency axis is set to coincide with the light pulse leading frequency. The results were normalized so that the maximum is equal to 1.

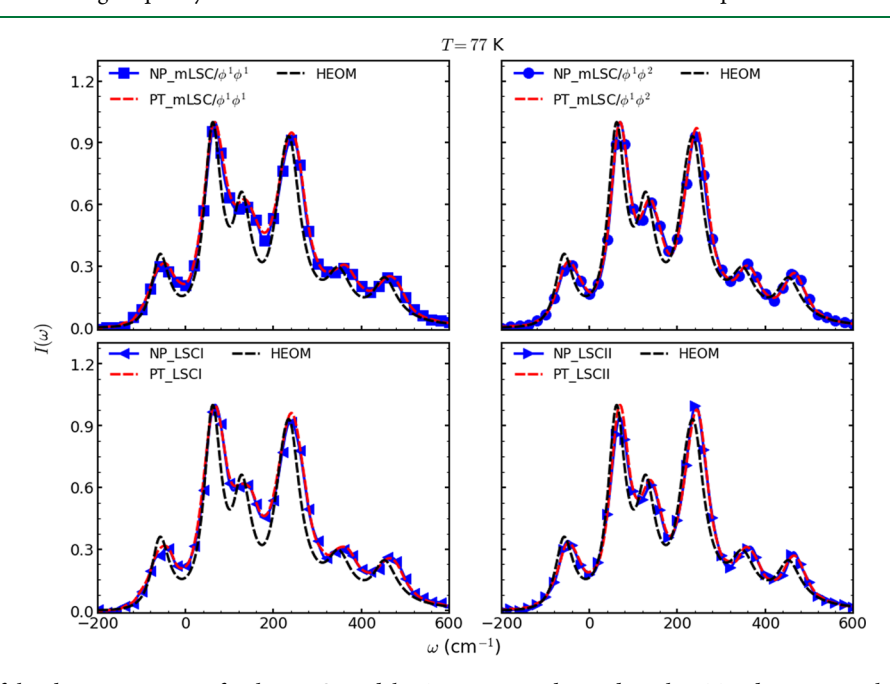


Figure 9. Comparison of the absorption spectra for the FMO model at T = 77 K, as obtained via the PT and NP approaches, based on the indicated QC/MH methods. Also shown numerically the exact HEOM method results obtained via the PT approach. ⁹⁰ The origin of the frequency axis is set to coincide with the light pulse leading frequency. The results were normalized so that the maximum is equal to 1.

have several advantages over the PT approach: (1) It can account for the nonperturbative effects that could give rise to a dependence of the spectra on the width, shape, chirp, and intensity of the light pulse; (2) Population—coherence correlation functions calculated via the QC/MH methods are expected to be more accurate than the coherence—coherence correlation functions; and (3) The NP approach is particularly straightforward to extend to the case of nonlinear multidimensional spectroscopy.

The results show that among the QC/MH methods considered, the LSC-based methods can yield accurate and robust absorption spectra when treating the nuclear DOF as

classical is a valid approximation. Within the LSC-based methods, LSCII, mLSC/ $\phi^1\phi^2$, and mLSC/ $\phi^2\phi^2$ were observed to be somewhat more accurate than LSCI and mLSC/ $\phi^1\phi^1$. It was also observed that MF and SQC gave rise to larger discrepancies in comparison to the exact results. More specifically, peak positions were observed to be shifted when MF was used, while relative peak heights were observed to be challenging to reproduce via SQC. Thus, at least based on the results presented in this paper, the LSC-based methods, and in particular LSCII, mLSC/ $\phi^1\phi^2$, and mLSC/ $\phi^2\phi^2$, emerge as the methods of choice. However, additional testing will have to be conducted to determine the general validity of this statement.

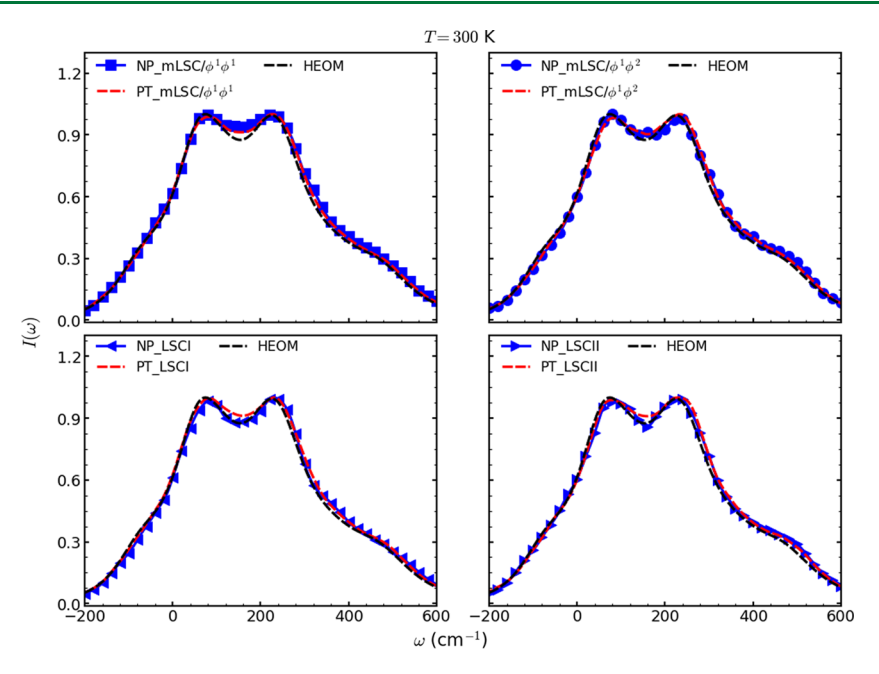


Figure 10. Comparison of the absorption spectra for the FMO model at T = 300 K, as obtained via the PT and NP approaches, based on the indicated QC/MH methods. Also shown numerically the exact HEOM method results obtained via the PT approach. ⁹⁰ The origin of the frequency axis is set to coincide with the light pulse leading frequency. The results were normalized so that the maximum is equal to 1.

Another interesting observation is the complementary nature of the Redfield method and QC/MH methods. More specifically, while the accuracy of the QC/MH methods improves as the nuclear DOF becomes slower and/or temperature is increased, that of the Redfield method improves as the nuclear DOF becomes faster and the temperature is decreased (as long as the coupling between nuclear and electronic DOF is sufficiently weak).

We view the accuracy and robustness of the LSC-based methods for calculating the absorption spectra presented in this paper as encouraging and indicative of their potential usefulness as general-purpose methods for simulating the spectra based on the all-atom anharmonic models of the complex molecular systems. The next natural step would be to extend the methodology to the calculation of the nonlinear time-resolved multidimensional spectra. Work on such an extension is currently underway and will be presented in a forthcoming separate publication.

A. APPENDIX: REDFIELD METHOD FOR CALCULATING THE LINEAR SPECTRA

The Redfield method for calculating the linear spectra used in this paper is similar to that described in ref 15. Below, we outline the main steps and assumptions underlying it.

The field-free dynamics within the Redfield method is described by a Markovian quantum master equation, also known as the Redfield equation. To this end, we cast the Frenkel excitonic Hamiltonian in the following system-bath form

$$\hat{H}_{M} = \hat{H}_{S} + \hat{H}_{B} + \hat{H}_{SB}$$

$$\hat{H}_{S} = \sum_{j=1}^{M} (\epsilon_{j} + \lambda_{j}) |j\rangle \langle j| + \sum_{j \neq j'}^{M} V_{j'j} |j'\rangle \langle j|$$

$$\hat{H}_{B} = \hat{H}_{0}$$

$$\hat{H}_{SB} = -\sum_{j=1}^{M} \sum_{a}^{N} \omega_{a}^{2} \hat{R}_{a} D_{a,j} |j\rangle \langle j| \equiv -\sum_{j=1}^{M} \sum_{a}^{N} C_{a,j} \hat{R}_{a} |j\rangle \langle j|$$
(50)

with $\lambda_j = (1/2) \sum_a^{N_n} \omega_a^2 D_{a,j}^2$. The Redfield quantum Master equation is obtained via the second-order perturbation theory with respect to $\hat{H}_{\rm SB}$ and assuming Markovity^{36,93,94}

$$\frac{\mathrm{d}}{\mathrm{d}t}\sigma_{JK}(t) = -\omega_{JK}\sigma_{JK}(t) - \sum_{M,N} \mathcal{R}_{JK,MN}\sigma_{MN}(t)$$
(51)

$$\mathcal{R}_{JK,MN} = \delta_{KN} \sum_{L} \tilde{C}_{JL,LM} + \delta_{JM} \sum_{L} \tilde{C}_{KL,LN}^{*} - \tilde{C}_{NK,JM}$$
$$- \tilde{C}_{MJ,KN}^{*} \tag{52}$$

$$\begin{split} \tilde{C}_{JK,MN} &= \frac{1}{\hbar^2} \int_0^\infty d\tau \ e^{i\omega_{NM}\tau} \ C_{JK,MN}(\tau) \\ &= \frac{1}{\hbar^2} \int_0^\infty d\tau \ e^{i\omega_{NM}\tau} \ Tr_B [\hat{\rho}_B^{eq} e^{i/\hbar \hat{H}_B \tau} \hat{H}_{JK}^{SB} e^{-i/\hbar \hat{H}_B \tau} \hat{H}_{MN}^{SB}] \end{split}$$
(53)

Here, J, K, M, and N stand for the eigenbasis of \hat{H}_S (not to be confused with j, k, m, and n, which correspond to the localized basis).

In the case of a harmonic bath, as in the Frenkel exciton models considered in this paper, $\tilde{C}_{JK,MN}$ can be evaluated analytically

$$\tilde{C}_{JK,MN} = \frac{1}{\hbar^2} \sum_{j,k} T_{j,J}^* T_{j,K} T_{k,M}^* T_{k,N} \tilde{C}_{jk,MN}; \ T_{j,J} = \langle j | J \rangle$$

$$\tilde{C}_{jk,MN} = \frac{\hbar}{\pi} \int_0^\infty d\tau \ e^{i\omega_{NM}\tau} \int_0^\infty d\omega \ J_{jk}(\omega) \left[\coth(\frac{1}{2}\omega\beta\hbar) \cos(\omega\tau) - i \sin(\omega\tau) \right]$$

Here, $J_{jk}(\omega) = \delta_{j,k}(1-\delta_{j,0})J(\omega)$. Applying the secular approximation, all terms that are not of the form $\mathcal{R}_{JK,KJ}$ are neglected.

The pulses are assumed to be in the strong impulsive limit with the field-matter interaction treated as a small perturbation to first order, so that the dynamics during the time period $(-\tau, 0)$ when the pulse is on is given by

$$\tilde{\sigma}(0) = \left(1 - \frac{i}{\hbar}\tilde{W}\tau\right)\tilde{\sigma}(-\tau)\left(1 + \frac{i}{\hbar}\tilde{W}\tau\right) \tag{55}$$

AUTHOR INFORMATION

Corresponding Author

Eitan Geva — Department of Chemistry, University of Michigan, Ann Arbor, Michigan 48109, United States; orcid.org/0000-0002-7935-4586; Email: eitan@umich.edu

Authors

Xing Gao – Department of Chemistry, University of Michigan, Ann Arbor, Michigan 48109, United States

Yifan Lai — Department of Chemistry, University of Michigan, Ann Arbor, Michigan 48109, United States

Complete contact information is available at: https://pubs.acs.org/10.1021/acs.jctc.0c00709

Notes

The authors declare no competing financial interest.

ACKNOWLEDGMENTS

X.G. thanks Tobias Kramer for providing the data of the FMO spectra calculated from HEOM in ref 90. X.G. also thanks Shuming Bai, Justin Provazza, and Jonathan H. Fetherolf for the helpful discussions. E.G. is grateful for the support from NSF via Grants CHE-1800325 and CHE-1663636. The computational resources and services for this project were provided by Advanced Research Computing at the University of Michigan, Ann Arbor.

■ REFERENCES

- (1) Mukamel, S. Principles of Nonlinear Optical Spectroscopy; Oxford: New York, 1995.
- (2) Jonas, D. M. Two-dimensional femtosecond spectroscopy. *Annu. Rev. Phys. Chem.* **2003**, *54*, 425–463.
- (3) Cho, M. Coherent two-dimensional optical spectroscopy. *Chem. Rev.* **2008**, *108*, 1331–1418.
- (4) Ogilvie, J. P.; Kubarych, K. J. Multidimensional electronic and vibrational spectroscopy: an ultrafast probe of molecular relaxation and reaction dynamics. *Adv. At., Mol., Opt. Phys.* **2009**, *57*, 249–321.
- (5) Mukamel, S.; Bakker, H. J. Preface: Special Topic on Multidimensional Spectroscopy. *J. Chem. Phys.* **2015**, *142*, 212101–212103.
- (6) Ka, B. J.; Geva, E. A nonperturbative calculation of nonlinear spectroscopic signals in liquid solution. *J. Chem. Phys.* **2006**, *125*, 214501–214514.
- (7) McRobbie, P. L.; Geva, E. A benchmark study of different methods for calculating one- and two-dimensional optical spectra. *J. Phys. Chem.* A **2009**, *113*, 10425–10434.

- (8) McRobbie, P. L.; Hanna, G.; Shi, Q.; Geva, E. Signatures of nonequilibrium solvation dynamics on multi-dimensional spectra. *Acc. Chem. Res.* **2009**, 42, 1299–1309.
- (9) Hanna, G.; Geva, E. Computational study of the one and two dimensional infrared spectra of a vibrational mode strongly coupled to its environment: Beyond the cumulant and Condon approximations. *J. Phys. Chem. B* **2008**, *112*, 12991–13004.
- (10) Hanna, G.; Geva, E. Isotope Effects on the Vibrational Relaxation and Multidimensional Infrared Spectra of the Hydrogen Stretch in a Hydrogen-Bonded Complex Dissolved in a Polar Liquid. *J. Phys. Chem.* B **2008**, *112*, 15793–15800.
- (11) Hanna, G.; Geva, E. Multi-dimensional spectra via the mixed quantum-classical Liouville method: Signatures of nonequilibrium dynamics. *J. Phys. Chem. B* **2009**, *113*, 9278–9288.
- (12) Hanna, G.; Geva, E. Computational study of the signature of hydrogen-bond strength on the infrared spectra of a hydrogen-bonded complex dissolved in a polar liquid. *Chem. Phys.* **2010**, *370*, 201.
- (13) Hanna, G.; Geva, E. Signature of Nonadiabatic Transitions on the Pump-Probe Infrared Spectra of a Hydrogen-Bonded Complex Dissolved in a Polar Solvent: A Computational Study. *J. Phys. Chem. B* **2011**, *115*, 5191–5200.
- (14) Baiz, C. R.; Kubarych, K. J.; Geva, E.; et al. Two-dimensional infrared spectroscopy of dimanganese decacarbonyl and its photoproducts: An ab-initio study. *J. Phys. Chem. A* **2009**, *113*, 9617.
- (15) Baiz, C. R.; Kubarych, K. J.; Geva, E. Molecular theory and simulation of coherence transfer in metal carbonyls and its signature on multidimensional infrared spectra. *J. Phys. Chem. B* **2011**, *115*, 5322–5339
- (16) Kwac, K.; Geva, E. Mixed Quantum-Classical Molecular Dynamics Study of the Hydroxyl Stretch in Methanol/Carbon-Tetrachloride Mixtures II: Excited State Hydrogen Bonding Structure and Dynamics, Infrared Emission Spectrum and Excited State Life-Time. J. Phys. Chem. B 2012, 116, 2856–2866.
- (17) Kwac, K.; Geva, E. A Mixed Quantum-Classical Molecular Dynamics Study of the Hydroxyl Stretch in Methanol/Carbon Tetrachloride Mixtures III: Nonequilibrium Hydrogen-Bond Dynamics and Infrared Pump-Probe Spectra. *J. Phys. Chem. B* **2013**, *117*, 7737–7749.
- (18) Kwac, K.; Geva, E. A Mixed Quantum-Classical Molecular Dynamics Study of anti-Tetrol and syn-Tetrol Dissolved in Liquid Chloroform: Hydrogen-Bond Structure and Its Signature on the Infrared Absorption Spectrum. *J. Phys. Chem. B* **2013**, *117*, 9996—10006.
- (19) Kwac, K.; Geva, E. A Mixed Quantum-Classical Molecular Dynamics Study of anti-Tetrol and syn-Tetrol Dissolved in Liquid Chloroform II: Infrared Emission Spectra, Vibrational Excited-State Life-Times and Nonequilibrium Hydrogen-Bond Dynamics. *J. Phys. Chem. B* **2013**, *117*, 14457–14467.
- (20) Bai, S.; Xie, W.; Zhu, L.; Shi, Q. Calculation of absorption spectra involving multiple excited states: Approximate methods based on the mixed quantum classical Liouville equation. *J. Chem. Phys.* **2014**, *140*, No. 084105.
- (21) Gruenbaum, S. M.; Loring, R. F. Semiclassical mean-trajectory approximation for nonlinear spectroscopic response functions. *J. Chem. Phys.* **2008**, *129*, No. 124510.
- (22) Petit, A. S.; Subotnik, J. E. Appraisal of surface hopping as a tool for modeling condensed phase linear absorption spectra. *J. Chem. Theory Comput.* **2015**, *11*, 4328–4341.
- (23) Jain, A.; Petit, A. S.; Anna, J. M.; Subotnik, J. E. Simple and Efficient Theoretical Approach To Compute 2D Optical Spectra. *J. Phys. Chem. B* **2019**, *123*, 1602–1617.
- (24) Van Der Vegte, C.; Dijkstra, A.; Knoester, J.; Jansen, T. Calculating two-dimensional spectra with the mixed quantum-classical ehrenfest method. *J. Phys. Chem. A* **2013**, *117*, 5970–5980.
- (25) Tempelaar, R.; van der Vegte, C. P.; Knoester, J.; Jansen, T. L. Surface hopping modeling of two-dimensional spectra. *J. Chem. Phys.* **2013**, *138*, No. 164106.

- (26) Provazza, J.; Segatta, F.; Garavelli, M.; Coker, D. F. Semiclassical path integral calculation of nonlinear optical spectroscopy. *J. Chem. Theory Comput.* **2018**, *14*, 856–866.
- (27) Richter, M.; Fingerhut, B. P. Simulation of multi-dimensional signals in the optical domain: Quantum-classical feedback in nonlinear exciton propagation. *J. Chem. Theory Comput.* **2016**, *12*, 3284–3294.
- (28) Tamura, H.; Burghardt, I.; Tsukada, M. Exciton Dissociation at Thiophene/Fullerene Interfaces: The Electronic Structures and Quantum Dynamics. *J. Phys. Chem. C* **2011**, *115*, 10205–10210.
- (29) Lee, M. H.; Dunietz, B. D.; Geva, E. Calculation From First Principles of Intramolecular Golden-Rule Rate Constants for Photo-Induced Electron Transfer in Molecular Donor-Acceptor Systems. *J. Phys. Chem. C* **2013**, *117*, 23391–23401.
- (30) Lee, M. H.; Dunietz, B. D.; Geva, E. Calculation from First Principles of Golden-Rule Rate Constants for Photo-Induced Subphthalocyanine/Fullerene Interfacial Charge Transfer and Recombination in Organic Photovoltaic Cells. *J. Phys. Chem. C* **2014**, *118*, 9780–9789.
- (31) Lee, M. H.; Dunietz, B. D.; Geva, E. Donor-to-Donor vs. Donor-to-Acceptor Interfacial Charge Transfer States in the Phthalocyanine-Fullerene Organic Photovoltaic System. *J. Phys. Chem. Lett.* **2014**, 5, 3810–3816.
- (32) Lee, M. K.; Coker, D. F. Modeling Electronic-Nuclear Interactions for Excitation Energy Transfer Processes in Light-Harvesting Complexes. *J. Phys. Chem. Lett.* **2016**, *7*, 3171–3178.
- (33) Novoderezhkin, V. I.; Romero, E.; Dekker, J. P.; van Grondelle, R. Multiple Charge-Separation Pathways in Photosystem II: Modeling of Transient Absorption Kinetics. *ChemPhysChem* **2011**, *12*, 681–688.
- (34) Chandrasekaran, S.; Aghtar, M.; Valleau, S.; Aspuru-Guzik, A.; Kleinekathöfer, U. Influence of Force Fields and Quantum Chemistry Approach on Spectral Densities of BChl a in Solution and in FMO Proteins. *J. Phys. Chem. B* **2015**, *119*, 9995–10004.
- (35) Gottwald, F.; Ivanov, S. D.; Kühn, O. Applicability of the Caldeira-Leggett Model to Vibrational Spectroscopy in Solution. *J. Phys. Chem. Lett.* **2015**, *6*, 2722–2727.
- (36) Nitzan, A. Chemical Dynamics in Condensed Phases; Oxford University Press: New York, 2006.
- (37) Wang, H.; Thoss, M. Quantum Dynamical Simulation of Electron-Transfer Reactions in an Anharmonic Environment. *J. Phys. Chem. A* **2007**, *111*, 10369–10375.
- (38) López-López, S.; Martinazzo, R.; Nest, M. Benchmark calculations for dissipative dynamics of a system coupled to an anharmonic bath with the multiconfiguration time-dependent Hartree method. *J. Chem. Phys.* **2011**, *134*, 094102–094108.
- (39) Hsieh, C.-Y.; Kapral, R. Correlation Functions in Open Quantum-Classical Systems. *Entropy* **2014**, *16*, 200–220.
- (40) Kwac, K.; Geva, E. A Mixed Quantum-Classical Molecular Dynamics Study of the Hydroxyl Stretch in Methanol/Carbon Tetrachloride Mixtures: Equilibrium Hydrogen-Bond Structure and Dynamics at the Ground State and the Infrared Absorption Spectrum. *J. Phys. Chem. B* **2011**, *115*, 9184–9194.
- (41) Loring, R. F. Mean-trajectory approximation for electronic and vibrational-electronic nonlinear spectroscopy. *J. Chem. Phys.* **2017**, *146*, No. 144106.
- (42) Polley, K.; Loring, R. F. Two-dimensional vibronic spectra from classical trajectories. *J. Chem. Phys.* **2019**, *150*, No. 164114.
- (43) Provazza, J.; Coker, D. F. Communication: Symmetrical quasiclassical analysis of linear optical spectroscopy. *J. Chem. Phys.* **2018**, *148*, 181102—181104.
- (44) Meyer, H.-D.; Miller, W. H. A classical analog for electronic degrees of freedom in nonadiabatic collision processes. *J. Chem. Phys.* **1979**, *70*, 3214–3223.
- (45) Stock, G.; Thoss, M. Semiclassical Description of Nonadiabatic Quantum Dynamics. *Phys. Rev. Lett.* **1997**, *78*, 578–581.
- (46) Sun, X.; Wang, H.; Miller, W. H. Semiclassical theory of electronically nonadiabatic dynamics: Results of a linearized approximation to the initial value representation. *J. Chem. Phys.* **1998**, *109*, No. 7064.

- (47) Wang, H.; Song, X.; Chandler, D.; Miller, W. H. Semiclassical study of electronically nonadiabatic dynamics in the condensed-phase: Spin-boson problem with Debye spectral density. *J. Chem. Phys.* **1999**, 110, 4828–4840.
- (48) Nassimi, A.; Bonella, S.; Kapral, R. Analysis of the quantum-classical Liouville equation in the mapping basis. *J. Chem. Phys.* **2010**, *133*, No. 134115.
- (49) Swenson, D. W. H.; Levy, T.; Cohen, G.; Rabani, E.; Miller, W. H. Application of a semiclassical model for the second-quantized many-electron Hamiltonian to nonequilibrium quantum transport: The resonant level model. *J. Chem. Phys.* **2011**, *134*, 164103–164109.
- (50) Kelly, A.; van Zon, R.; Schofield, J.; Kapral, R. Mapping quantum-classical Liouville equation: Projectors and trajectories. *J. Chem. Phys.* **2012**, *136*, 084101–084113.
- (51) Cotton, S. J.; Miller, W. H. Symmetrical windowing for quantum states in quasi-classical trajectory simulations: Application to electronically non-adiabatic processes. *J. Chem. Phys.* **2013**, *139*, No. 234112.
- (52) Cotton, S. J.; Miller, W. H. Symmetrical Windowing for Quantum States in Quasi-Classical Trajectory Simulations. *J. Phys. Chem. A* **2013**, *117*, 7190–7194.
- (53) Cotton, S. J.; Igumenshchev, K.; Miller, W. H. Symmetrical windowing for quantum states in quasi-classical trajectory simulations: Application to electron transfer. *J. Chem. Phys.* **2014**, *141*, 084104–084111.
- (54) Cotton, S. J.; Miller, W. H. A Symmetrical Quasi-Classical Spin-Mapping Model for the Electronic Degrees of Freedom in Non-Adiabatic Processes. *J. Phys. Chem. A* **2015**, *119*, 12138–12145.
- (55) Cotton, S. J.; Miller, W. H. The Symmetrical Quasi-Classical Model for Electronically Non-Adiabatic Processes Applied to Energy Transfer Dynamics in Site-Exciton Models of Light-Harvesting Complexes. J. Chem. Theory Comput. 2016, 12, 983–991.
- (56) Cotton, S. J.; Miller, W. H. A new symmetrical quasi-classical model for electronically non-adiabatic processes: Application to the case of weak non-adiabatic coupling. *J. Chem. Phys.* **2016**, *145*, 144108—144117.
- (57) Saller, M. A. C.; Kelly, A.; Richardson, J. O. On the identity of the identity operator in nonadiabatic linearized semiclassical dynamics. *J. Chem. Phys.* **2019**, *150*, 071101–071108.
- (58) Saller, M. A. C.; Kelly, A.; Richardson, J. O. Improved population operators for multi-state nonadiabatic dynamics with the mixed quantum-classical mapping approach. *Faraday Discuss.* **2020**, 221, 150–167.
- (59) Tao, G. Electronically Nonadiabatic Dynamics in Singlet Fission: A Quasi-Classical Trajectory Simulation. *J. Phys. Chem. C* **2014**, *118*, 17299–17305.
- (60) Tao, G. A multi-state trajectory method for non-adiabatic dynamics simulations. *J. Chem. Phys.* **2016**, *144*, 094108–094109.
- (61) Tao, G.; Shen, N. Mapping State Space to Quasiclassical Trajectory Dynamics in Coherence-Controlled Nonadiabatic Simulations for Condensed Phase Problems. *J. Phys. Chem. A* **2017**, *121*, 1734–1747.
- (62) Tao, G. Nonadiabatic Dynamics of Hydrogen Diffusion on Cu(001): Classical Mapping Model with Multistate Projection Window in Real Space. *ChemPhysChem* **2019**, 62, No. 39.
- (63) Liu, J. A unified theoretical framework for mapping models for the multi-state Hamiltonian. *J. Chem. Phys.* **2016**, *145*, 204105–204115.
- (64) Kananenka, A. A.; Hsieh, C.-Y.; Cao, J.; Geva, E. Nonadiabatic Dynamics via the Symmetrical Quasi-Classical Method in the Presence of Anharmonicity. *J. Phys. Chem. Lett.* **2018**, *9*, 319–326.
- (65) He, X.; Liu, J. A new perspective for nonadiabatic dynamics with phase space mapping models. *J. Chem. Phys.* **2019**, *151*, 024105–024122.
- (66) Gao, X.; Saller, M. A. C.; Liu, Y.; Kelly, A.; Richardson, J. O.; Geva, E. Benchmarking Quasiclassical Mapping Hamiltonian Methods for Simulating Electronically Nonadiabatic Molecular Dynamics. *J. Chem. Theory Comput.* **2020**, *16*, 2883–2895.

- (67) Liu, Y.; Gao, X.; Lai, Y.; Mulvihill, E.; Geva, E. Electronic Dynamics through Conical Intersections via Quasiclassical Mapping Hamiltonian Methods. *J. Chem. Theory Comput.* **2020**, *16*, 4479–4488.
- (68) Meyer, H.-D.; Gatti, F.; Worth, G. A. Multidimensional Quantum Dynamics; MCTDH Theory and Applications; John Wiley & Sons, 2009.
- (69) Miller, W. H.; Cotton, S. J. Classical molecular dynamics simulation of electronically non-adiabatic processes. *Faraday Discuss*. **2016**, *195*, 9–30.
- (70) Kananenka, A. A.; Sun, X.; Schubert, A.; Dunietz, B. D.; Geva, E. A comparative study of different methods for calculating electronic transition rates. *J. Chem. Phys.* **2018**, *148*, 102304–102313.
- (71) Thoss, M.; Stock, G. Mapping approach to the semiclassical description of nonadiabatic quantum dynamics. *Phys. Rev. A* **1999**, *59*, 64–79.
- (72) Stock, G.; Müller, U. Flow of zero-point energy and exploration of phase space in classical simulations of quantum relaxation dynamics. *J. Chem. Phys.* **1999**, *111*, 65–76.
- (73) Miller, W. H. The semiclassical initial value representation: A potentially practical way for adding quantum effects to classical molecular dynamics simulations. *J. Phys. Chem. A* **2001**, *105*, 2942–2955.
- (74) Ananth, N.; Venkataraman, C.; Miller, W. H. Semiclassical description of electronically nonadiabatic dynamics via the initial value representation. *J. Chem. Phys.* **2007**, *127*, No. 084114.
- (75) Kim, H.; Nassimi, A.; Kapral, R. Quantum-classical Liouville dynamics in the mapping basis. *J. Chem. Phys.* **2008**, *129*, No. 084102.
- (76) Miller, W. H.; Cotton, S. J. Communication: Wigner functions in action-angle variables, Bohr-Sommerfeld quantization, the Heisenberg correspondence principle, and a symmetrical quasi-classical approach to the full electronic density matrix. *J. Chem. Phys.* **2016**, *145*, 081102—081105.
- (77) Cotton, S. J.; Liang, R.; Miller, W. H. On the adiabatic representation of Meyer-Miller electronic-nuclear dynamics. *J. Chem. Phys.* **2017**, *147*, No. 064112.
- (78) Wang, H.; Thoss, M.; Miller, W. H. Forward-backward initial value representation for the calculation of thermal rate constants for reactions in complex molecular systems. *J. Chem. Phys.* **2000**, *112*, No. 47.
- (79) Shi, Q.; Geva, E. A relationship between semiclassical and centroid correlation functions. *J. Chem. Phys.* **2003**, *118*, 8173–8184.
- (80) Shi, Q.; Geva, E. Nonradiative electronic relaxation rate constants from approximations based on linearizing the path-integral forward-backward action. *J. Phys. Chem. A* **2004**, *108*, 6109–6116.
- (81) Runeson, J. E.; Richardson, J. O. Spin-mapping approach for nonadiabatic molecular dynamics. *J. Chem. Phys.* **2019**, *151*, No. 044119.
- (82) Mulvihill, E.; Gao, X.; Liu, Y.; Schubert, A.; Dunietz, B. D.; Geva, E. Combining the mapping Hamiltonian linearized semiclassical approach with the generalized quantum master equation to simulate electronically nonadiabatic molecular dynamics. *J. Chem. Phys.* **2019**, *151*, No. 074103.
- (83) Cotton, S. J.; Miller, W. H. Trajectory-adjusted electronic zero point energy in classical Meyer-Miller vibronic dynamics: Symmetrical quasiclassical application to photodissociation. *J. Chem. Phys.* **2019**, *150*, No. 194110.
- (84) Skinner, J. L.; Andersen, H. C.; Fayer, M. D. Correlation function analysis of coherent optical transients and flouresence from a quasi-two-level system. *Phys. Rev. A* **1981**, *24*, No. 1994.
- (85) Wang, H.; Thoss, M. Theoretical study of ultrafast photoinduced electron transfer processes in mixed-valence systems. *J. Phys. Chem. A* **2003**, *107*, 2126–2136.
- (86) Ishizaki, A.; Fleming, G. R. On the adequacy of the Redfield equation and related approaches to the study of quantum dynamics in electronic energy transfer. *J. Chem. Phys.* **2009**, *130*, 234110–234119.
- (87) Chen, L.; Zheng, R.; Jing, Y.; Shi, Q. Simulation of the two-dimensional electronic spectra of the Fenna-Matthews-Olson complex using the hierarchical equations of motion method. *J. Chem. Phys.* **2011**, *134*, No. 194508.

- (88) Sharp, L. Z.; Egorova, D.; Domcke, W. Efficient and accurate simulations of two-dimensional electronic photon-echo signals: illustration for a simple model of the Fenna–Matthews–Olson complex. *J. Chem. Phys.* **2010**, *132*, No. 014501.
- (89) Hein, B.; Kreisbeck, C.; Kramer, T.; Rodríguez, M. Modelling of oscillations in two-dimensional echo-spectra of the Fenna–Matthews–Olson complex. *New J. Phys.* **2012**, *14*, No. 023018.
- (90) Kramer, T.; Noack, M.; Reinefeld, A.; Rodríguez, M.; Zelinskyy, Y. Efficient calculation of open quantum system dynamics and timeresolved spectroscopy with distributed memory HEOM (DM-HEOM). J. Comput. Chem. **2018**, 39, 1779–1794.
- (91) Berkelbach, T. pyrho: A python package for reduced density matrix techniques. https://github.com/berkelbach-group/pyrho.
- (92) Fetherolf, J. H.; Berkelbach, T. C. Linear and nonlinear spectroscopy from quantum master equations. *J. Chem. Phys.* **2017**, 147, No. 244109.
- (93) Redfield, A. G. On the theory of relaxation processes. *IBM J. Res. Dev.* **1957**, *1*, 19.
- (94) Breuer, H.-P.; Petruccione, F. The Theory of Open Quantum Systems; Oxford Press: Oxford, 2002.